Article

Preparation of PVA/SA-FMB Microspheres and Their Adsorption of Cr(VI) in Aqueous Solution

Jinlong Zuo [1], Jin Ren [1], Liming Jiang [1], Chong Tan [1], Junsheng Li [1], Zhi Xia [1,*] and Wei Wang [2,*]

[1] School of Food Science and Engineering, Harbin University of Commerce, Harbin 150028, China; 101760@hrbcu.edu.cn (J.Z.); 15103558302@163.com (J.R.); 101716@hrbcu.edu.cn (L.J.); 102776@hrbcu.edu.cn (C.T.); 101719@hrbcu.edu.cn (J.L.)

[2] State Key Laboratory of Urban Water Resource and Environment, School of Environment, Harbin Institute of Technology, Harbin 150090, China

[*] Correspondence: 102820@hrbcu.edu.cn (Z.X.); wangweirs@hit.edu.cn (W.W.)

Abstract: Biochar, a carbon-dense material known for its substantial specific surface area, remarkable porosity, diversity of functional groups, and cost-effective production, has garnered widespread acclaim as a premier adsorbent for the elimination of heavy metal ions and organic contaminants. Nevertheless, the application of powdered biochar is hindered by the challenges associated with its separation from aqueous solutions, and without appropriate management, it risks becoming hazardous waste. To facilitate its use as an immobilization medium, biochar necessitates modification. In this investigation, sodium alginate, celebrated for its superior gelation capabilities, was amalgamated with polyvinyl alcohol to bolster mechanical robustness, thereby embedding biochar to formulate sodium alginate biochar microspheres (PVA/SA-FMB). A meticulously designed response surface methodology experiment was employed to ascertain the optimal synthesis conditions for PVA/SA-FMB. Characterization outcomes unveiled a highly developed surface abundant in functional groups and confirmed the successful incorporation of iron ions. Adsorption trials revealed that at a temperature of 25 °C and a pH of 2, the adsorption capacity of PVA/SA-FMB for Cr(VI) was 13.7 mg/g within the initial 30 min, reaching an equilibrium capacity of 26.03 mg/g after 1440 min. Notably, the material sustained a Cr(VI) removal efficiency exceeding 90% across five cycles, underscoring its rapid and effective Cr(VI) eradication performance. Kinetic and isothermal adsorption analyses suggested that the adsorption of Cr(VI) adheres to a pseudo-second-order kinetic model and the Freundlich isotherm, indicative of monolayer adsorption dominated by reaction mechanisms. X-ray photoelectron spectroscopy (XPS) analysis inferred that the adsorption mechanism predominantly encompasses electrostatic attraction, redox processes, and complex formation.

Keywords: biochar; sodium alginate microspheres; adsorption; Cr(VI)

1. Introduction

The adsorption technique emerges as a notably efficient and convenient strategy for the removal of metal ions, consistent with established theories encompassing adsorption thermodynamics, kinetics, and isotherms. This method integrates chemisorption, involving complexation reactions, with physisorption, characterized by electrostatic interactions between heavy metal ions and adsorbents [1]. The critical challenge lies in identifying adsorbents that exhibit both high capacity and selectivity for metal ion removal. Presently, the array of adsorbents spans activated carbon, biomass, graphene oxide, various carbon-based materials, nanoparticles, and synthetic polymers [2]. Despite their utility, traditional adsorbents like biochar suffer from limitations such as limited adsorption capacity and slow kinetic rates. Recent advancements have focused on enhancing the activity of adsorbents using methods like chemical structure modification, crosslinking, and grafting.

Sodium alginate (SA), a naturally occurring, water-soluble polysaccharide extracted from kelp or brown algae, stands out as an environmentally friendly option due to its cost-effectiveness, non-toxicity, biodegradability, and biocompatibility [3,4]. It is composed of β-D mannuronic acid (ManA) and α-L guluronic acid (GulA) in variable proportions and sequences, offering exceptional gelling properties. However, its application in heavy metal adsorption is often hindered by limited porosity, mechanical strength, stability, and thermal resistance, necessitating modifications to improve its performance characteristics. The chemical structure of SA, depicted in Figure 1, illustrates its potential for modification and enhancement in adsorption applications.
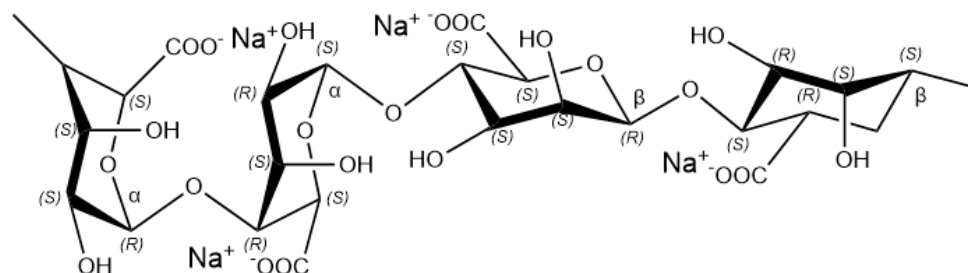

Figure 1. Chemical structure formula of sodium alginate.

Crosslinking significantly transforms the solubility characteristics of sodium alginate (SA) and augments the mechanical robustness of the adsorbent by fostering a three-dimensional (3D) network [5]. This advancement in crosslinking technology has bolstered the SA matrix, creating a durable 3D framework that plays a crucial role in the more efficacious entrapment of heavy metal ions. The deliberate integration of biochar not only amplifies the composite's structural resilience but also elevates its environmental compatibility, positioning it as a potent candidate in the heavy metal ion adsorption arena. This enhancement process is facilitated by crosslinking agents, which foster the linkage of macromolecular entities to SA via diverse mechanisms, including ion exchange, polyelectrolyte crosslinking, hydrogen bonding, hydrophobic interactions, condensation polymerization, chemical grafting polymerization, and free radical polymerization. These methodologies ingeniously modify SA's inherent solubility and bolster its mechanical attributes [6,7]. Prominent crosslinking agents encompass calcium chloride, glutaraldehyde, epichlorohydrin, formaldehyde, and concentrated sulfuric acid.

In ion crosslinking, the guluronic acid (GulA) units in SA predominantly serve as the binding locales. The carboxylate groups on these units are adept at chelating with divalent or polyvalent metal ions, which supplant the sodium ions (Na+) in various SA molecular strands, thereby interlinking them and crafting a hydrogel network [8]. Calcium chloride is particularly esteemed as a crosslinking agent due to the optimal size of the Ca(II) ions for interacting with the -OH and -COOH groups on the polysaccharide chains. This synergy, coupled with the surface charge density of Ca(II), culminates in the creation of a formidable physical crosslinking lattice [9]. The ratio of mannuronic acid (ManA) to guluronic acid (GulA) monomers in SA critically influences the characteristics of the resultant hydrogels, with an elevated GulA content generally leading to enhanced mechanical properties.

Covalent crosslinking capitalizes on the -OH and -COOH groups on the SA molecular chain as anchorage points. Crosslinking agents such as glutaraldehyde and polyethylene glycol (PEG-200) are deployed, resulting in the genesis of hydrogels. This technique further refines the structural and functional efficacy of SA across various domains [10].

Embedding modification entails the judicious selection of appropriate filler materials for integration into SA, aiming to surmount challenges associated with fine material loss and recovery, while simultaneously boosting adsorption efficiency and environmental adaptability. The overall performance of the resultant composite material is intimately linked to the type, amount, and concentration of the incorporated substances. Filler materials commonly employed include activated carbon, biochar, graphene, and carbon

nanotubes [11,12]. When embedded into SA, these substances significantly enhance the composite's structural and functional traits, rendering it more apt for diverse applications, especially those necessitating efficient adsorption properties.

The profusion of hydroxyl and carboxyl groups in SA endows it with a pronounced affinity for adsorbing heavy metal ions. By amalgamating biochar, renowned for its porous architecture and extensive surface area, with SA, a composite has been developed that transcends the limitations of conventional adsorbents, such as inferior capacity and sluggish kinetics, while showcasing superior adsorption capabilities. This study delves into the composite's morphology, structure, elemental composition, and functional groups, alongside scrutinizing its adsorption dynamics under varying conditions to unravel the mechanisms underlying Cr(VI) adsorption.

2. Materials and Methods

2.1. Experimental Reagents

Corn straw biomass was collected from the experimental field (from Harbin University of Commerce); Ferric chloride(FeCl$_3$, AR) from Tianjin Beilian Fine Chemicals Development Co., Ltd. (Tianjin, China); Sodium alginate(SA, AR) from Qingdao Mingyue Seaweed Group Co., Ltd. (Qingdao, China); Polyvinyl alcohol(PVA, AR) from Shanxi Sanwei Group Co., Ltd. (Linfen, China); Calcium carbonate(CaCO$_3$, AR) from Xilong Science Co., Ltd. (Shantou, China); Hydrochloric acid(HCl, AR) from Nanjing Chemical Reagent Co., Ltd. (Nanjing, China); Sodium hydroxide(NaOH, AR) from Tianjin Continental Chemical Reagent Factory (Tianjin, China).

2.2. Preparation of PVA/SA-FMB Microsphere

2.2.1. Preparation of the FMB

A measured quantity of 10 g of corn stover biomass was measured and placed in a 100 mL beaker, and then immersed in 100 mL of 2 mol/L FeCl$_3$ solution, maintaining a solid-to-liquid ratio of 1:10 (g/mL). This mixture underwent magnetic stirring for 30 min, followed by a 30 min water bath at 80 °C. Afterward, the biomass was separated from the solution, dried, and then pyrolyzed at a temperature of 500 °C in a nitrogen (N$_2$) atmosphere. Once cooled to room temperature, the biomass was washed repeatedly with deionized (DI) water to remove chloride ions and then dried at 80 °C. This process yielded FeCl$_3$-modified corn stover biochar, referred to as FeCl$_3$-modified biochar (FMB), which was subsequently sealed and stored for future use.

2.2.2. Preparation of PVA/SA Solution

Polyvinyl alcohol (PVA) was dissolved in boiling water until it formed a clear solution, which was then cooled to room temperature. A total of 0.6% of SA was then added to this PVA solution and water-bathed at 60 °C for 90 min to obtain the PVA/SA solution.

2.2.3. Preparation of PVA/SA-FMB Microspheres

Biochar was ultrasonically dispersed in a PVA/SA-FMB solution, to which 0.6 g of CaCO$_3$ was added and magnetically stirred for an hour. This solution was then dripped into a FeCl$_3$ solution to form ionic crosslinked gel balls, which were hardened for 24 h. The gel balls were washed with distilled water to remove surface Fe^{3+} ions, treated in HCl solution for 2 h to create porous PVA/SA-FMB microspheres, and finally dried and stored at 40 °C.

2.3. Optimization of Parameters for the Preparation of PVA/SA-FMB Microspheres

The study optimized crucial parameters for preparing PVA/SA-FMB microspheres, focusing on SA concentration, the SA-to-PVA ratio, CaCO$_3$ concentration, crosslinking solution concentration, and pickling time. Using response surface methodology (RSM), we examined how these factors influenced Cr(VI) adsorption using PVA/SA-FMB microspheres to determine the optimal preparation conditions.

2.4. Characterization and Principle of Materials

- Element composition analysis: An element analyzer was utilized to quantitatively assess the elemental composition of biochar, focusing primarily on carbon (C) and oxygen (O).
- X-ray diffraction (XRD) analysis: The phase structure of the materials was studied using a EVASTAR Y2 X-ray diffractometer from Suzhou Ivan Zhitong (Suzhou, China), covering a test range of $2\theta = 10$–$90°$.
- Surface area and pore size analysis (BET): The pore structures of different biochars have their own characteristics. The specific surface area, total pore volume, and average pore diameter of the test samples were analyzed using the ChemStation-001 type nitrogen adsorption–desorption instrument from mainland China (Zhejiang, China) to examine the types of adsorption–desorption curves.
- Scanning electron microscope (SEM): In this experiment, the morphology of the samples was observed using a Supra55 scanning electron microscope from the German company Zeiss (Jena, Germany), with an EHT of 15 KV. Before testing, the samples were thoroughly dried and sputter-coated with gold.
- X-ray photoelectron spectroscopy (XPS): In this experiment, the elemental composition and valence state information of the samples were characterized using the ESCALAB 250 X-ray photoelectron spectrometer(Thermo Fisher Scientific Company, Waltham, MA, USA). The Al Kα radiation was 1486.6 eV, with a vacuum level better than 5×10^{-10} mbar.
- Fourier transform infrared spectroscopy (FTIR): The structure of the samples was characterized using the VERTEX 80 Infrared-Raman spectrometer from the German company Bruker (Berlin, Germany), with a spectral range of 4000–400 cm^{-1} and a resolution of 0.07 cm^{-1}.

2.5. Evaluation of Adsorption Properties

Single factor adsorption experiment: Different quantities of adsorbent were added to 50 mL solutions of varying concentrations of Cr(VI). The pH of the Cr(VI) solution was adjusted, and the mixture was subjected to a constant temperature water bath oscillation at 25 °C and 140 r/min for 24 h. Post-experiment, the solutions were filtered through a 0.22 μm membrane, the Cr(VI) concentration in each sample was measured by UV-Vis spectrophotometry, and the removal rate and amount were calculated.

Adsorption kinetics experiment: A total of 0.1 g of adsorbent was mixed with 50 mL of 50 mg/L Cr(VI) solution and oscillated in a 25 °C, followed by 140 r/min constant temperature water bath at various intervals (0, 10, 30, 60, 90, 120, 180, 360, 540, 720, and 1440 min). The absorbance of residual Cr(VI) was measured to determine the removal rate and adsorption capacity.

Isothermal adsorption experiment: Cr(VI) solutions of pH 2 and concentrations ranging from 10 mg/L to 100 mg/L were prepared, with 0.1 g of adsorbent added to each. These were oscillated in a 25 °C, followed by 140 r/min constant temperature water bath for 24 h and then filtered through a 0.22 μm membrane to evaluate the removal rate and adsorption capacity.

Adsorption cycle regeneration experiment: A total of 0.1 g of adsorbent was added to a 50 mL, 50 mg/L Cr(VI) solution (pH 2) and oscillated under the same conditions as above for 24 h. After reaching adsorption saturation, the adsorbent was placed in a 50 mL eluent (0.1 mol/L NaOH) and oscillated again to release Cr(VI). The regenerated adsorbent's efficiency in removing Cr(VI) was then assessed.

3. Results and Discussion

3.1. Optimization of Preparation Parameters for PVA/SA-FMB Microspheres

3.1.1. Analysis of Single Factor Test Results

1. The effect of SA concentration on the preparation of PVA/SA-FMB microspheres

Figure 2 underscores the paramount importance of SA concentration in the morphogenesis of PVA/SA-FMB microspheres, delineating a concentration-dependent impact on their structural integrity and formation efficacy. At suboptimal concentrations below 0.6% (*w/v*), the resultant low viscosity of the solution is detrimental to effective microsphere formation, culminating in the development of flocculent structures and microspheres with compromised durability, prone to disintegration during adsorption processes. This phenomenon is attributed to an inadequate SA quantity, insufficient to counteract PVA agglomeration [13,14]. In contrast, concentrations surpassing 0.6% (*w/v*) induce an excessive viscosity, obstructing the syringe extrusion process and leading to the formation of microspheres with irregular shapes and the potential for syringe nozzle obstructions.
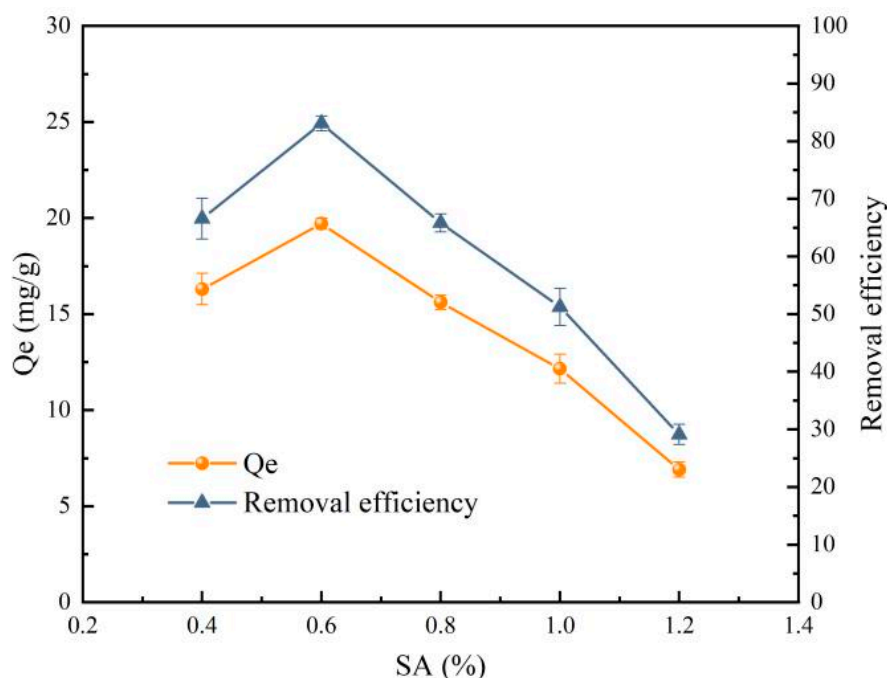

Figure 2. Influence of SA concentration on adsorption of Cr(VI) by PVA/SA-FMB microspheres (C_0 = 50 mg/L, V = 50 mL, pH = 2.0, T = 25 °C).

The optimal formation of microspheres, marked by uniformity and spherical morphology, is realized at an SA concentration of 0.6% (*w/v*). This observation highlights the criticality of precise SA concentration in achieving the desired physical properties of PVA/SA-FMB microspheres, balancing between solution viscosity and syringe extrudability. It establishes a threshold concentration for SA that ensures the production of structurally robust and morphologically consistent microspheres, essential for their application in environmental remediation, particularly for the adsorption of heavy metal ions.

2. Effect of PVA concentration on the preparation of PVA/SA-FMB microspheres

In the synthesis of PVA/SA-FMB microspheres, PVA is instrumental in augmenting the mechanical resilience of the microspheres. An insufficiency of PVA compromises their structural fortitude, rendering them incapable of withstanding the rigors of the adsorption process. Conversely, a PVA concentration exceeding 3% enhances mechanical properties but concurrently impairs the adsorption efficiency for Cr(VI), likely due to the resultant denser

microsphere structure which impedes mass transfer [15]. Figure 3 illustrates that a PVA concentration of 2.4% (*w/v*) strikes an optimal equilibrium between mechanical robustness and adsorptive capacity, facilitating the most effective Cr(VI) removal in PVA/SA-FMB microspheres. This concentration allows for a substantial adsorption capacity of 22 mg/g for Cr(VI) following a 24 h oscillatory adsorption procedure, underscoring the microspheres' proficiency under these conditions.
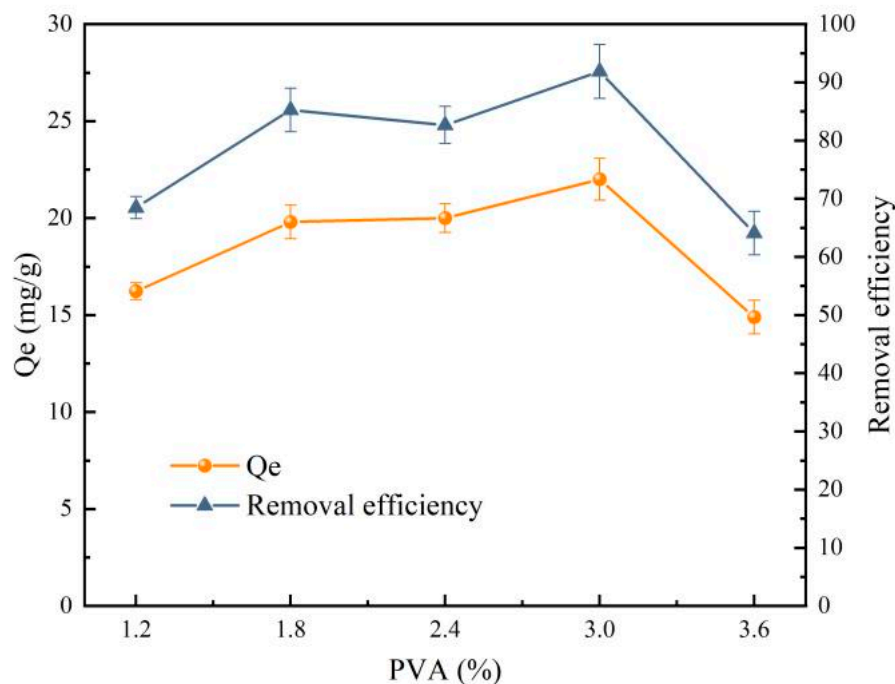

Figure 3. Influence of PVA concentration on adsorption of Cr(VI) by PVA/SA-FMB microspheres (C_0 = 50 mg/L, V = 50 mL, pH = 2.0, T = 25 °C).

3.   Influence of FMB mass on the preparation of PVA/SA-FMB microspheres

Figure 4 delineates a discernible pattern in the adsorptive dynamics of PVA/SA-FMB microspheres. Initially, an increase in FMB mass correlates positively with enhanced Cr(VI) adsorption capacity, highlighting FMB's pivotal contribution to the adsorption mechanism amidst constituents such as SA, PVA, and calcium carbonate ($CaCO_3$). Nevertheless, this upward trajectory in adsorption capacity plateaus and subsequently diminishes upon exceeding an FMB mass of 0.3 g. This downturn is attributed to the complications in achieving uniform FMB dispersion within the solution at higher concentrations. Excess FMB not only poses challenges like syringe clogging during microsphere fabrication but also compromises microsphere integrity. Optimal adsorption efficiency, therefore, necessitates a judicious balance in FMB content, ensuring both effective Cr(VI) adsorption and the structural cohesiveness of the microspheres.

4.   Influence of $CaCO_3$ mass on the preparation of PVA/SA-FMB microspheres

Investigating the impact of varied $CaCO_3$ masses on Cr(VI) adsorption using PVA)/SA- FMB microspheres and experiments with $CaCO_3$ masses of 0.3 g, 0.6 g, 0.9 g, 1.2 g, and 1.5 g were conducted. Figure 5 illustrates an initial enhancement in the microspheres' adsorptive performance with increasing $CaCO_3$ mass, attributable to the intensified interactions between Ca(II) ions and the guluronic (G) units of SA. However, a notable stabilization in the adsorption rate at approximately 20 mg/g is observed beyond a $CaCO_3$ mass of 0.6 g. This leveling effect is linked to the achievement of an equilibrium state between dehydration and water reabsorption processes, facilitating stable gel formation [16]. Furthermore, under consistent hydrochloric acid (HCl) concentration and exposure duration, the internal microporosity of the PVA/SA-FMB microspheres

remains unchanged beyond the threshold $CaCO_3$ mass required for optimal chemical interaction with HCl.
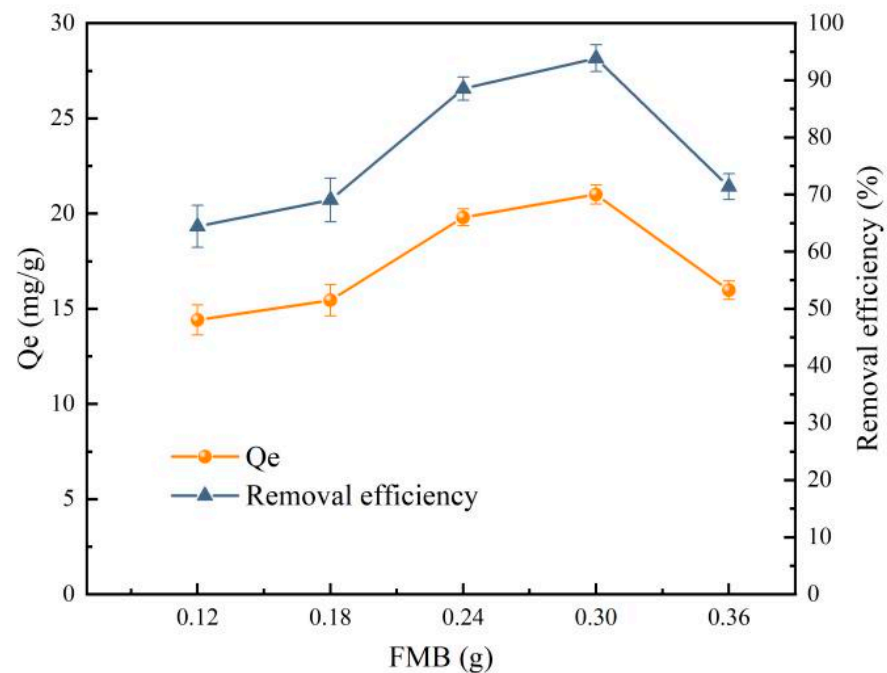

Figure 4. Influence of FMB mass on adsorption of Cr(VI) by PVA/SA-FMB microspheres (C_0 = 50 mg/L, V = 50 mL, pH = 2.0, T = 25 °C).

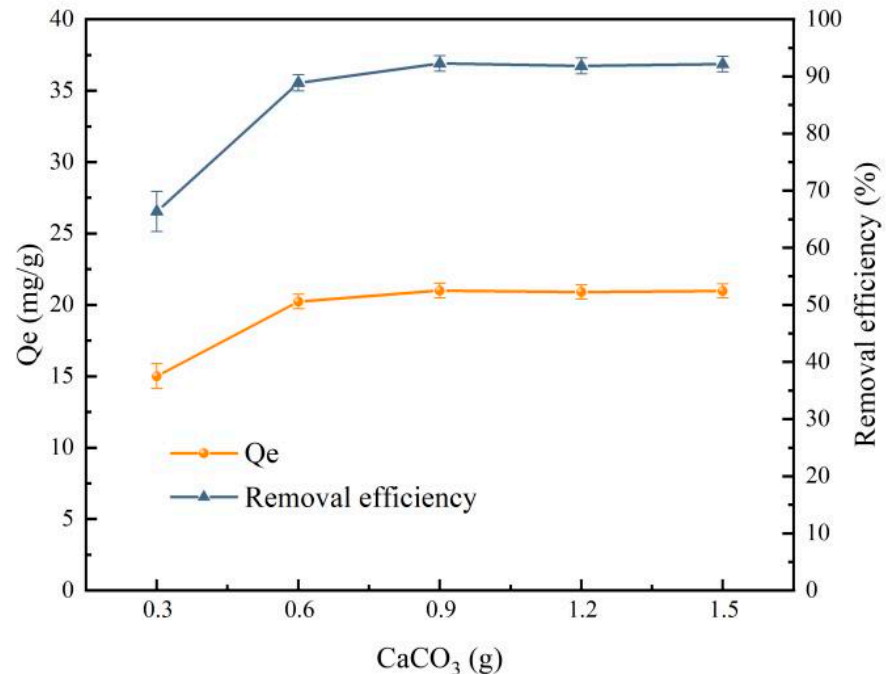**Figure 5.** Influence of $CaCO_3$ mass on adsorption of Cr(VI) by PVA/SA-FMB microspheres (C_0 = 50 mg/L, m = 0.1 g, V = 50 mL, pH = 2.0, T = 25 °C).

3.1.2. Establishment and Analysis of the RSM Model

1. Design of RSM test

Employing the Box–Behnken response surface design [17], the study delineated four critical determinants in the synthesis of PVA)/SA-FMB microspheres: SA concentration (A),

PVA concentration (B), FMB mass (C), and CaCO$_3$ mass (D), targeting adsorption capacity as the response variable. A structured four-factor, three-level response surface analysis was executed, as encapsulated in Table 1, to establish the paramount preparation conditions.

Table 1. Factors and levels of response surface test.

Variables	Code	Horizontal Coding		
		−1	0	1
SA/%	A	0.4	0.6	0.8
PVA/%	B	2.4	3	3.6
CaCO$_3$/g	C	0.3	0.6	0.9
FMB/g	D	0.24	0.3	0.36

2. Establishment and analysis of the regression model

Adhering to the Box–Behnken design framework, this study scrutinized the Cr(VI) adsorption efficacy of PVA/SA-FMB microspheres under diverse composite conditions. Data accrued from these evaluations were meticulously analyzed to pinpoint the optimal parameters for microsphere synthesis, with outcomes tabulated in Table 2. This analysis confirmed that the interplay among the four scrutinized parameters adheres to a quadratic model. Consequently, the adsorption capacity (Qe) of the PVA/SA-FMB microspheres is quantitatively delineated by an equation comprising coded variables, as specified in Equation (1). Within this equation, a positive coefficient before a term delineates a synergistic influence, while a negative coefficient signifies an antagonistic impact.

$$Y = 25.32 + 0.46 \times A - B + 0.42 \times C - 0.45 \times D - 0.27 \times A \times B + 0.36 \times A \times C - 1.43 \times A \times D \\ + 0.18 \times B \times C + 0.69 \times B \times D - 0.67C \times D - 4.27 \times A^2 - 1.20 \times B^2 - 5.34 \times C^2 - 0.57 \times D^2 \tag{1}$$

Table 2. Design and results of response surface test.

No.	A	B	C	D	Adsorption Amount of Cr(VI)/mg/g		No.	A	B	C	Adsorption Amount of Cr(VI)/mg/g	Adsorption Amount of Cr(VI)/mg/g	
					Test Value	Predicted Value						Test Value	Predicted Value
1	−1	−1	0	0	18.95	19.41	16	0	1	1	0	19.05	19.08
2	1	−1	0	0	20.71	20.86	17	−1	0	−1	0	15.59	15.2
3	−1	1	0	0	18.86	19.36	18	1	0	−1	0	15.64	15.38
4	1	1	0	0	19.53	19.74	19	−1	0	1	0	15.81	15.31
5	0	0	−1	−1	18.9	18.77	20	1	0	1	0	17.31	16.95
6	0	0	1	−1	20.63	20.95	21	0	−1	0	−1	25.12	24.98
7	0	0	−1	1	18.87	19.22	22	0	1	0	−1	23.52	23.01
8	0	0	1	1	17.92	18.71	23	0	−1	0	1	22.96	22.71
9	−1	0	0	−1	18.89	19.04	24	0	1	0	1	24.1	23.49
10	1	0	0	−1	22.5	22.82	25	0	0	0	0	24.96	25.32
11	−1	0	0	1	21.23	21.01	26	0	0	0	0	24.88	25.32
12	1	0	0	1	19.12	19.06	27	0	0	0	0	26.14	25.32
13	0	−1	−1	0	18.76	18.83	28	0	0	0	0	25.47	25.32
14	0	1	−1	0	17.51	17.88	29	0	0	0	0	25.15	25.32
15	0	−1	1	0	19.59	19.31							

The precision of the model was quantified using the correlation coefficient R^2, with values closer to 1 indicating a tighter concordance between model predictions and empirical observations. For this model, an R^2 of 0.9855 was reported, signifying a notably high accuracy in its predictive capability. The disparity between predicted outcomes and actual data was observed to be less than 0.2, affirming the model's reliability. A detailed juxtaposition of actual measured values against the predictions derived from the model's equation is presented in Table 2.

3. Response regression analysis

The model's validity was established through F-value and *p*-value analysis, as detailed in Table 3, highlighting the significance of SA concentration, ferric oxide-modified biochar quality, and PVA concentration as impactful model terms. ANOVA results underscored a coefficient of determination (R^2) at 0.9855 and an adjusted R^2 (R^2adj) of 0.9711, elucidating that the model accounts for 97.11% of the response variability. The model's precision, quantified at 25.804, far exceeds the benchmark of 4, reinforcing its appropriateness. With a Coefficient of Variation (CV) at 2.65%, markedly below the 10% threshold, the model's reliability and accuracy are affirmed. These analytical outcomes collectively confirm the regression equation's robustness and its capacity to accurately predict experimental results, validating the model's applicability for determining the optimal synthesis parameters for PVA/SA-FMB microspheres.

Table 3. Results of response surface regression analysis.

Items	Sum of Squares	Degrees of Freedom	Mean Square	F-Value	*p*-Value	Significance
Model	221.27	14	15.8	85.33	<0.0001	**
A	3.5	1	3.5	18.88	0.0117	*
B	0.12	1	0.12	0.67	0.0836	
C	3.03	1	3.03	16.34	0.0187	**
D	2.67	1	2.67	14.43	0.0131	*
AB	1.54	1	1.54	8.29	0.3395	
AC	0.53	1	0.53	2.84	0.2048	
AD	7.08	1	7.08	38.22	0.0001	*
BC	0.13	1	0.13	0.69	0.5227	
BD	0.86	1	0.86	4.62	0.0245	*
CD	0.71	1	0.71	3.82	0.0276	*
A^2	92.01	1	92.01	496.79	<0.0001	**
B^2	6.98	1	6.98	37.7	<0.0001	**
C^2	136.42	1	136.42	736.54	<0.0001	**
D^2	0.41	1	0.41	2.2	0.0191	*
Residual	2.59	14	0.19			
Missing fitting item	1.54	10	0.15	0.58	0.4732	
Absolute error	1.05	4	0.26			
Total	223.86	28				

Note: $p < 0.01$, extremely significant "**"; $p < 0.05$, significant "*".

4. Optimized model response surface analysis

The three-dimensional (3D) response surface diagrams are instrumental in delineating the regression equation, offering a visual exposition of how each variable's response value correlates with its test value. Figures 6–8 display the response surface models for variables such as SA concentration, ferric oxide-modified biochar mass, $CaCO_3$ mass, and PVA concentration, illustrating their respective impacts on Cr(VI) adsorption rates. Notably, the contour shapes within these figures underscore the interactions between variable pairs [18].

Figure 6 elucidates the relationship between $CaCO_3$ mass and SA concentration with respect to Cr(VI) adsorption capacity. An increase in SA concentration from 0.4 wt% to 0.8 wt% leads to a peak in Cr(VI) adsorption rates at an SA concentration of 0.6 wt%, with an elliptical contour shape and a *p*-value of AD below 0.05 (0.0001) signifying a significant interaction between $CaCO_3$ mass and SA concentration on Cr(VI) adsorption.

Figure 7 showcases the impact of $CaCO_3$ mass and PVA concentration on Cr(VI) adsorption rates through response surface and contour lines. It reveals that increasing PVA concentration from 1.8 wt% to 3 wt%, with a constant $CaCO_3$ mass, leads to a decrease in Cr(VI) adsorption, underscoring the influence of PVA concentration. The elliptical contours and a *p*-value of 0.0245 (below 0.05) indicate a significant interaction between $CaCO_3$ mass and PVA concentration, emphasizing their critical role in modulating Cr(VI) adsorption rates.
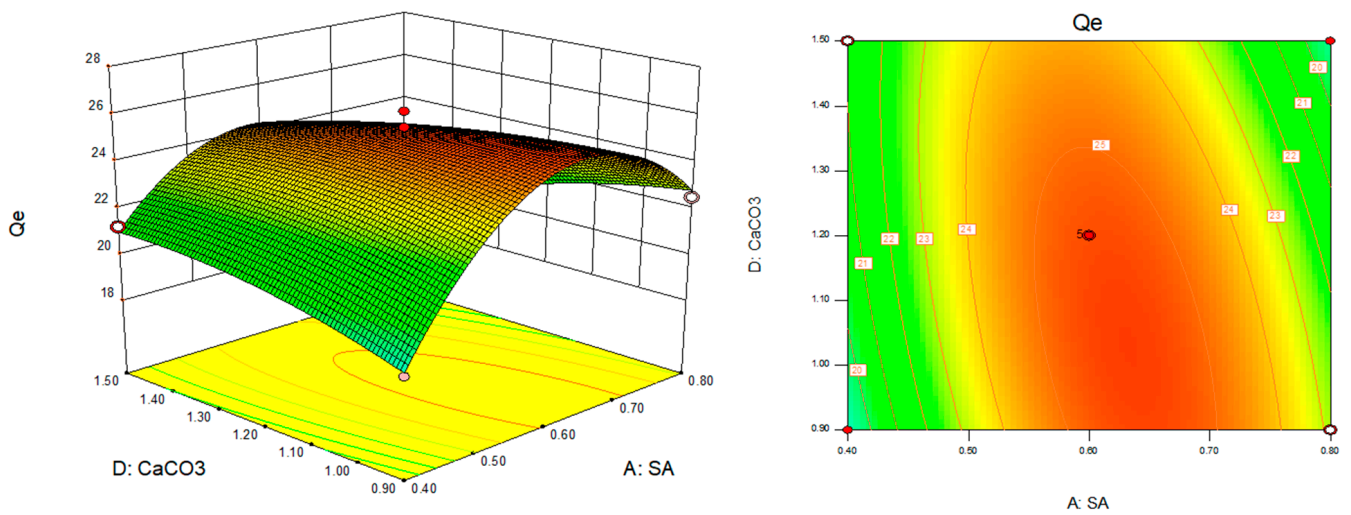
Figure 6. Response surfaces and contours of SA and PVA concentrations on Cr(VI) adsorption capacity.
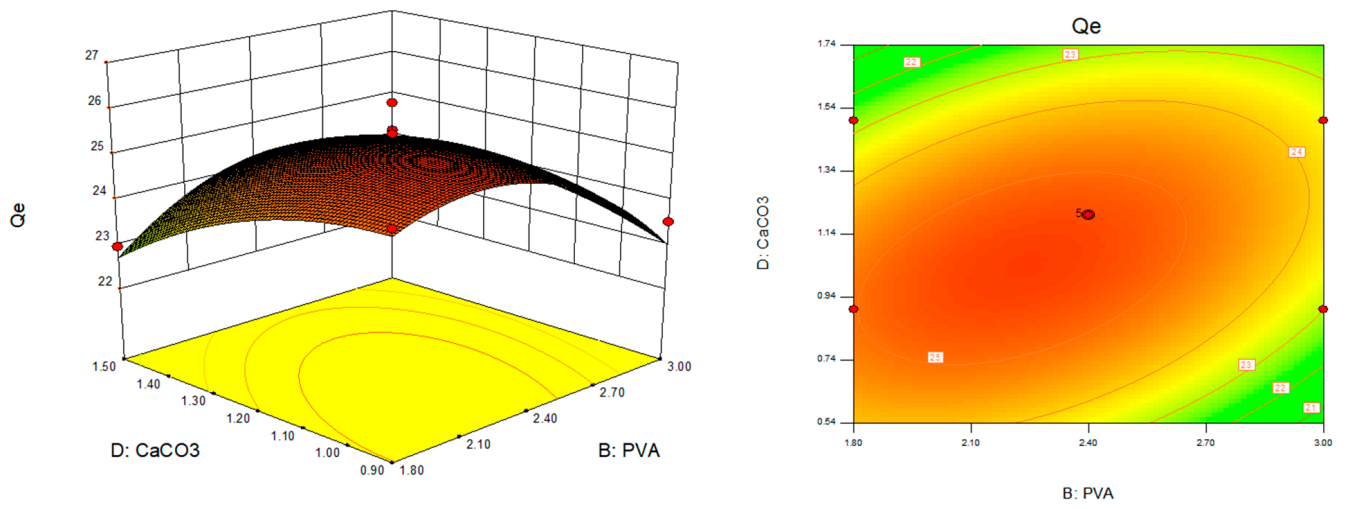

Figure 7. Response surfaces and contours of $CaCO_3$ mass and PVA concentration on Cr(VI) adsorption capacity.
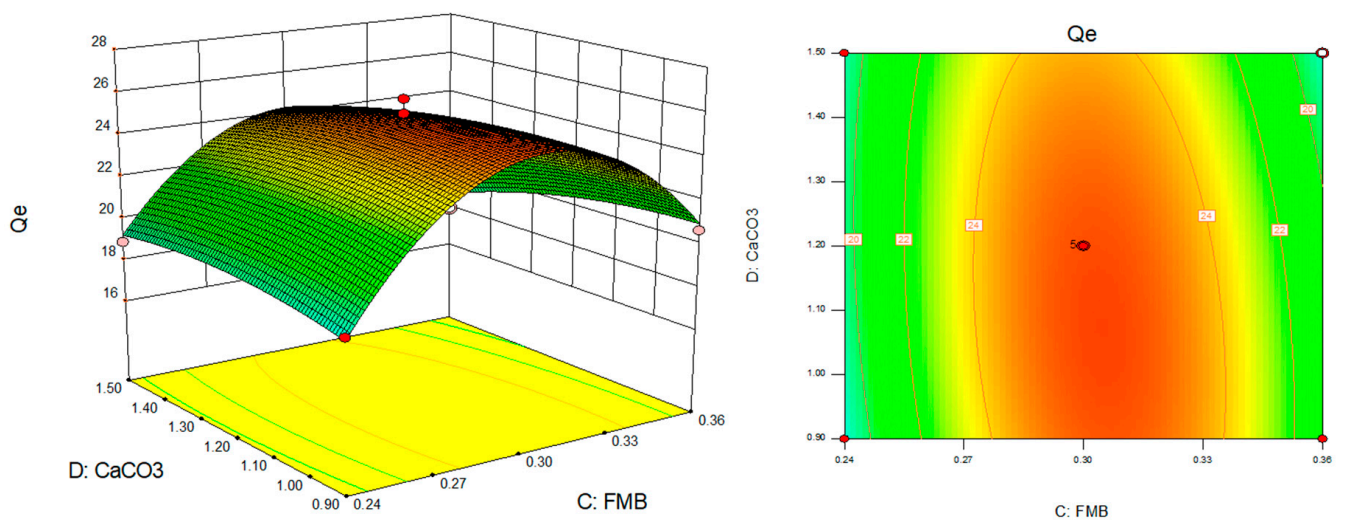

Figure 8. Response surfaces and contours of $CaCO_3$ mass and FMB mass on Cr(VI) adsorption capacity.

Figure 8 displays the response surface and contour lines representing the influence of $CaCO_3$ mass and FMB mass on the Qe for Cr(VI). According to the figure, the optimal adsorption rate of Cr(VI) occurs when the FMB mass is at 0.3 g. The elliptical shape of the contour lines and a *p*-value for the interaction (AD) of 0.0276, which is less than 0.05, indicate a significant interaction between the masses of $CaCO_3$ and FMB in affecting Cr(VI) adsorption. Furthermore, the analysis suggests that the interaction between SA concentration and PVA concentration does not significantly influence the efficiency of Cr(VI) removal.

The three-dimensional analysis provided a deeper insight into the interactions among different variables and their influence on achieving optimal conditions. The relative importance of the four response parameters affecting the Qe of Cr(VI) was established in the following order: $CaCO_3$ content, SA concentration, FMB quality, and PVA concentration. Using Design Expert 8.0 software for analysis, the optimal preparation conditions for PVA/SA-FMB microspheres to attain the highest Cr(VI) adsorption performance were determined. The ideal concentrations and amounts were found to be an SA concentration of 0.73 t%, a PVA concentration of 3 wt%, an FMB mass of 0.31 g, and a $CaCO_3$ concentration of 1 g. Under these conditions, the microspheres are expected to exhibit maximum efficiency in adsorbing Cr(VI) from solutions.

3.2. Characterization and Principle of the Materials

3.2.1. Analysis of Element Composition

The elemental composition analysis of PVA/SA-MB and PVA/SA-FMB is shown in Table 4. Based on the ratios of O/C and (O + N)/C, it was found that PVA/SA-FMB possesses higher polarity and hydrophilicity compared to PVA/SA-MB, further proving that the polarity and hydrophilicity of adsorptive materials are closely related to their adsorption performance.

Table 4. Elemental composition of biochar.

Samples	C	O	N	O/C	(O + N)/C
PVA/SA-MB	68.85	30.09	1.06	0.4370	0.4524
PVA/SA-FMB	24.07	73.89	2.04	3.0698	3.1545

3.2.2. X-ray Diffraction (XRD) Determination

X-ray diffraction (XRD) analysis on PVA/SA, PVA/SA-MB, and PVA/SA-FMB revealed significant structural alterations attributable to the embedding modification process (Figure 9). Pure SA displayed characteristic diffraction peaks at 2θ values of 13.5° and 21.5°, absent in both PVA/SA-MB and PVA/SA-FMB, indicating modifications in SA's structure post-embedding. PVA/SA-MB retained broad biochar-associated diffraction peaks around 2θ = 16–22°, suggesting the preservation of biochar's amorphous cellulose and hemicellulose structures. Conversely, PVA/SA-FMB exhibited distinct peaks at 2θ = 20.197°, 21.440°, and 29.649°, which aligned with Fe_2O_3 and FeO standards (PDF#21-0920 and PDF#74-1886) [19], denoting the incorporation of both divalent and trivalent iron forms, indicative of complex interactions enhancing adsorption capabilities.

3.2.3. Specific Surface Area (BET) and Pore Size Analysis

The nitrogen (N_2) adsorption–desorption isotherms of PVA/SA, PVA/SA-MB, and PVA/SA-FMB, as shown in Figures 10–12, are categorized as type IV according to the International Union of Pure and Applied Chemistry (IUPAC), suggesting mesoporous or macroporous structures within the microspheres. The initial sharp increase in adsorption at low pressures indicates monolayer adsorption, affirming the microporous nature of the microspheres. The emergence of a closed hysteresis loop in the mid- to high-pressure ranges, classified as H3 type, signifies the presence of slit-like pores due to particle layering.

Pore size analysis via Non-Local Density Functional Theory (NLDFT) revealed that microspheres incorporating biochar exhibited a pronounced micro and mesopore structure within the 0–10 nm range, enhancing the overall pore architecture of PVA/SA. Conversely, the shift from larger pores in the 10–100 nm range to biochar's smaller pores during embedding improves adsorption efficacy. The specific surface area, an essential parameter for adsorbent evaluation, underscores the adsorptive capacity and delineates the intrinsic properties of the adsorbent materials, reflecting both their advantages and limitations in adsorption applications. (See Table 5).
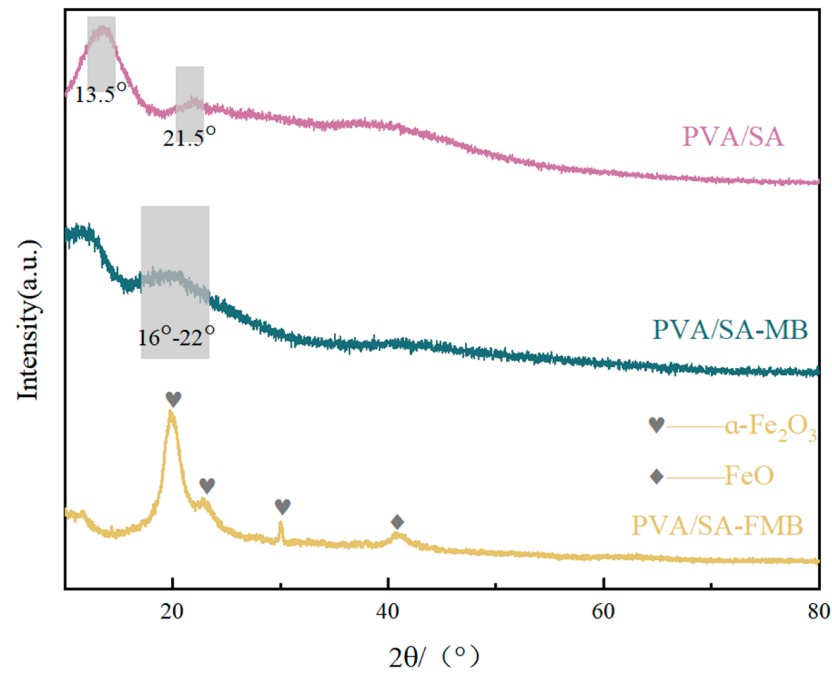
Figure 9. X-ray diffraction pattern of biochar.
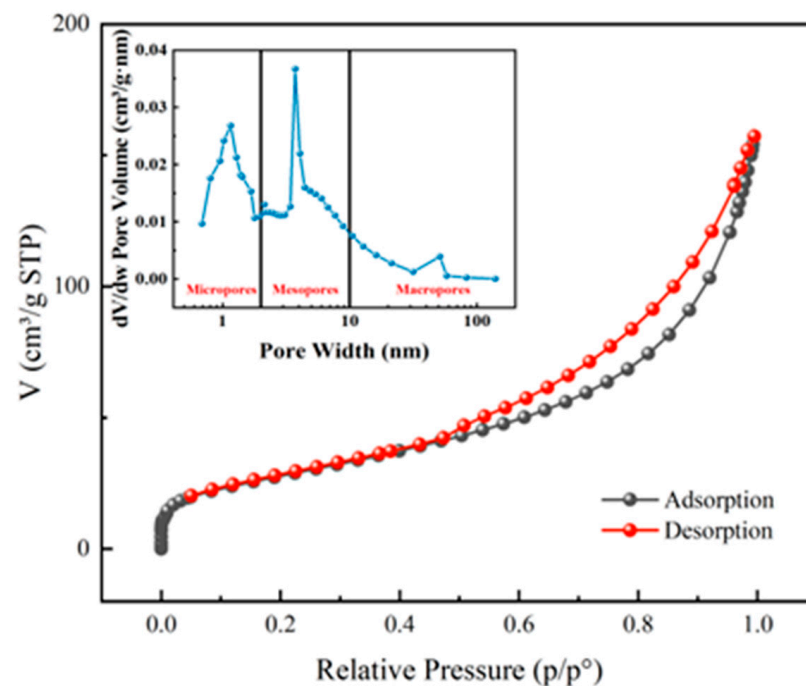
Figure 10. N$_2$ adsorption and desorption isotherm and pore size distribution of PVA/SA.
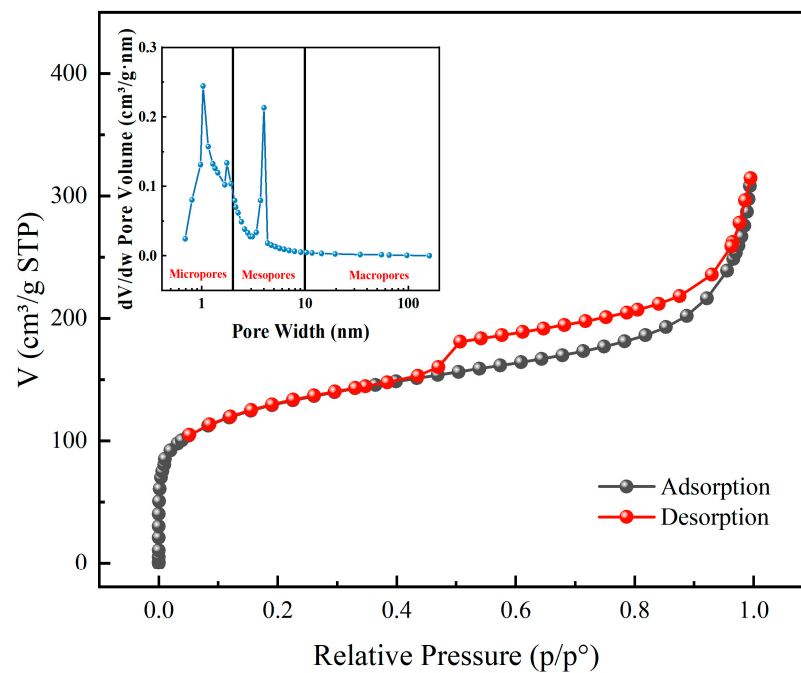
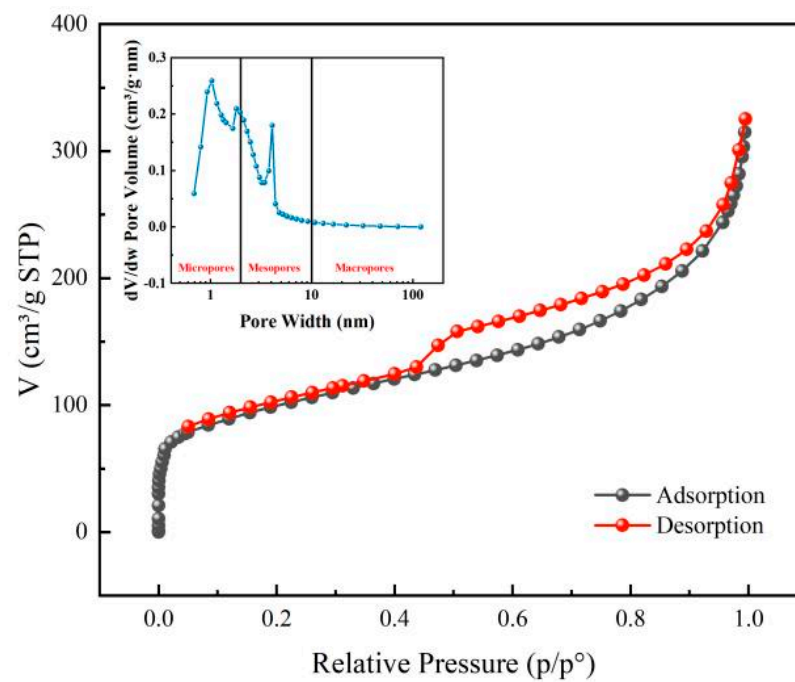**Figure 11.** N$_2$ adsorption–desorption isotherm and pore size distribution of PVA/SA-MB.

Figure 12. N$_2$ adsorption–desorption isotherm and pore size distribution of PVA/SA-FMB.

Table 5. Characterization parameters of specific surface area and pore structure of microspheres.

Sample	BET Surface Area/($m^2 \cdot g^{-1}$)	V/<1.1 nm ($cm^3 \cdot g^{-1}$)	V/<1.1 nm ($cm^3 \cdot g^{-1}$)	Average Pore Diameter/(nm)
PVA/SA	100.6120	0.00289	0.228412	9.21610
PVA/SA-MB	441.7465	0.09947	0.4146567	4.05464
PVA/SA-FMB	344.2612	0.16795	0.451204	5.32073

3.2.4. Scanning Electron Microscope (SEM) Determination

SEM was employed to analyze the morphology of modified microspheres, showcasing their unique advantages. Figure 13 displays the SEM images of MB, PVA/SA, PVA/SA-MB, and PVA/SA-FMB microspheres.
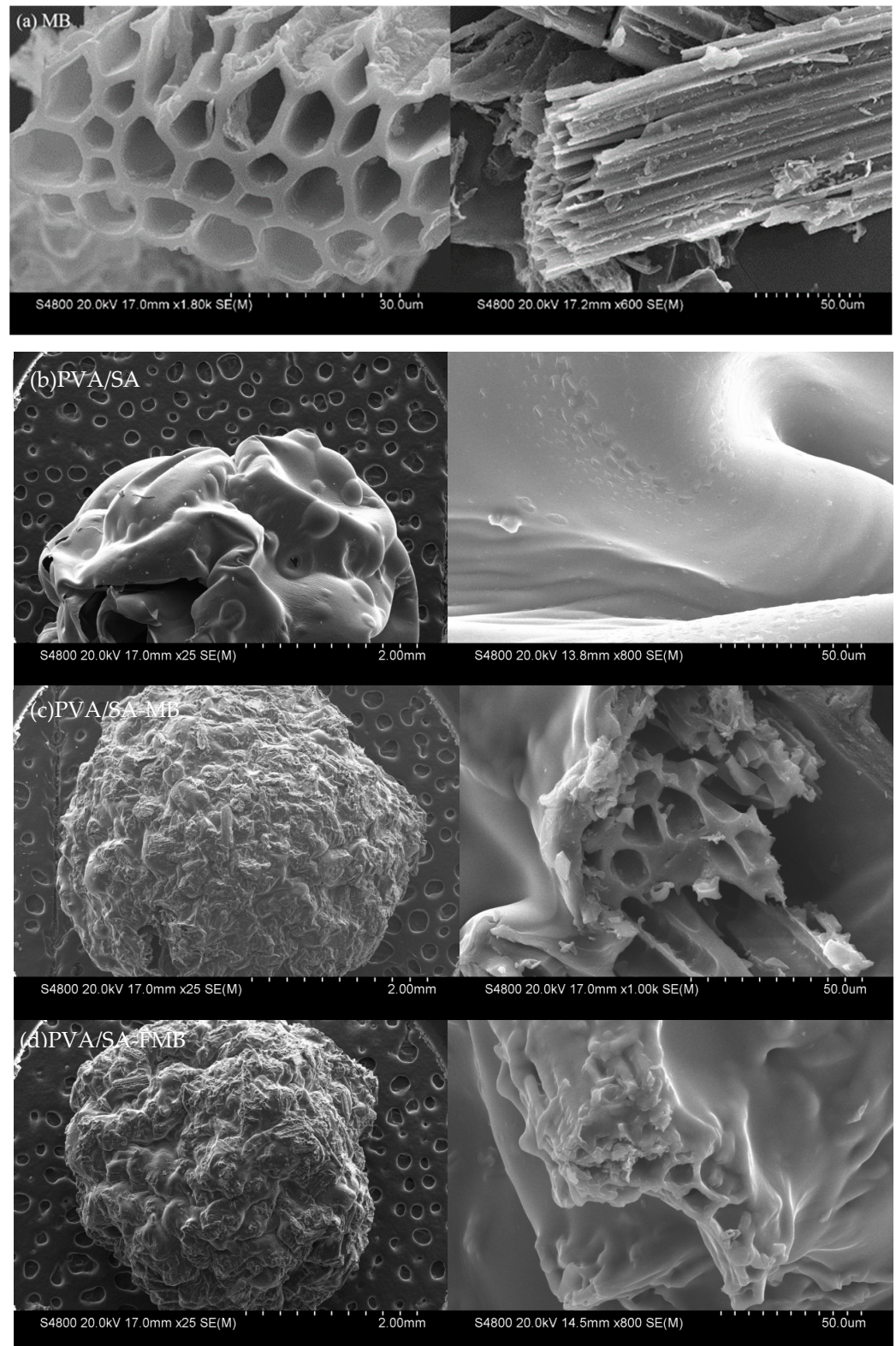

Figure 13. SEM of microspheres (**a**) MB; (**b**) PVA/SA; (**c**) PVA/SA-MB; (**d**) PVA/SA-FMB.

For PVA/SA microspheres, a smooth surface with irregular folds and limited porosity is observed, attributed to the cohesive nature of PVA. The integration of biochar, however, markedly transforms the microspheres' surface and internal architecture, introducing a rougher texture and a proliferation of pores, including distinctive honeycomb-like structures. This transformation results from biochar interfering with the original hydrogen bonds of PVA while establishing new interactions with its hydroxyl groups, thereby diminishing PVA's adhesive effect. Such alterations suggest that biochar-enhanced microspheres feature an expanded specific surface area and a more intricate pore network, augmenting their adsorptive capacity. Biochar serves as an efficient medium, augmenting the adsorption sites on PVA/SA, which in turn amplifies the microspheres' overall adsorptive performance. Specifically, PVA/SA-FMB microspheres display more pronounced and complex pore configurations than PVA/SA-MB, corroborating with the BET surface area and pore size distribution findings.

3.2.5. X-ray Photoelectron Spectroscopy (XPS) Determination

Figure 14b elucidates the C1s peak fitting in the XPS spectra of PVA/SA-MB and PVA/SA-FMB microspheres, diverging from pure biochar. This peak encompasses a spectrum of carbon bonds, notably C-C/C-H, C-O, and C=O/O-C=O, with significant absorptions at C-O and C=O, signaling the presence of carbon–oxygen compounds.

Furthermore, Figure 14c delineates the Fe 2p spectral peak in PVA/SA-FMB microspheres' XPS spectrum, demonstrating a broader and distorted peak. This feature suggests the oxidation state of iron, affirming the effective amalgamation of SA with iron. Before the adsorption of Cr(VI) by PVA/SA-FMB, five absorption peaks appeared in Figure 14c. binding energies at 710.87 eV and 724.25 eV denote divalent iron, whereas 714.76 eV and 727.56 eV correspond to trivalent iron, alongside a satellite peak at 716.9 eV linked to the Fe(II) Fe 2p3/2 orbital, indicating complex iron valence states within the microspheres.

3.2.6. Fourier Transform Infrared Spectroscopy (FTIR) Determination

Figure 15 showcases the FTIR spectra for SA and its composite microspheres (PVA/SA, PVA/SA-MB, and PVA/SA-FMB), covering the 400–4000 cm^{-1} wavelength range. SA's spectrum, displaying characteristic peaks at specified wavelengths, confirms its structural attributes [20]. The composite microspheres exhibit functional group structures akin to SA, indicating the retention of SA's chemical properties through the compounding process.

Notable across all materials is the peak at 3300 cm^{-1}, signifying -OH stretching vibrations from hydroxyl groups. The 2800–3000 cm^{-1} range highlights C-H stretching vibrations, while the 1600 cm^{-1} peak suggests C=O stretching in ketones and acids. Peaks at 1024 cm^{-1} and 818 cm^{-1} are attributed to C-H bending vibrations, with the 1420 cm^{-1} peak indicating carboxyl group stretching.

Differential features in the composite microspheres include enhanced absorption peaks at 1680 cm^{-1} and 473 cm^{-1}, indicative of a rise in oxygen-containing functional groups. The 1680 cm^{-1} peak, more prominent in PVA/SA-MB and PVA/SA-FMB, is linked to C=C stretching, suggesting biochar's role in augmenting the aromatic structure. The 473 cm^{-1} peak, associated with Fe-O bonds, underscores the successful integration of FeCl$_3$ and biochar FMB, particularly evidenced in PVA/SA-FMB, marking the effective crosslinking of Fe-containing groups in the microsphere synthesis.

3.3. Evaluation of Adsorption Properties

3.3.1. Adsorption Single Factor Experiment

1. Initial concentration

Figure 16 illustrates the impact of initial Cr(VI) concentration on the adsorption capacity of adsorbents, revealing an increase in adsorption capacity with rising Cr(VI) concentration at a stable temperature, alongside a reduction in removal rate. This pattern is ascribed to an augmented driving force necessary to counteract the mass transfer resistance of Cr(VI) across the aqueous–solid interface at elevated concentrations [21]. Notably,

PVA/SA-FMB demonstrates a pronounced adsorption capacity for Cr(VI), even at lower concentrations (10 mg/L), achieving up to 4.1 mg/g. This highlights PVA/SA-FMB's strong affinity for Cr(VI), underscoring its potential for effective Cr(VI) removal from aqueous solutions at minimal concentrations.
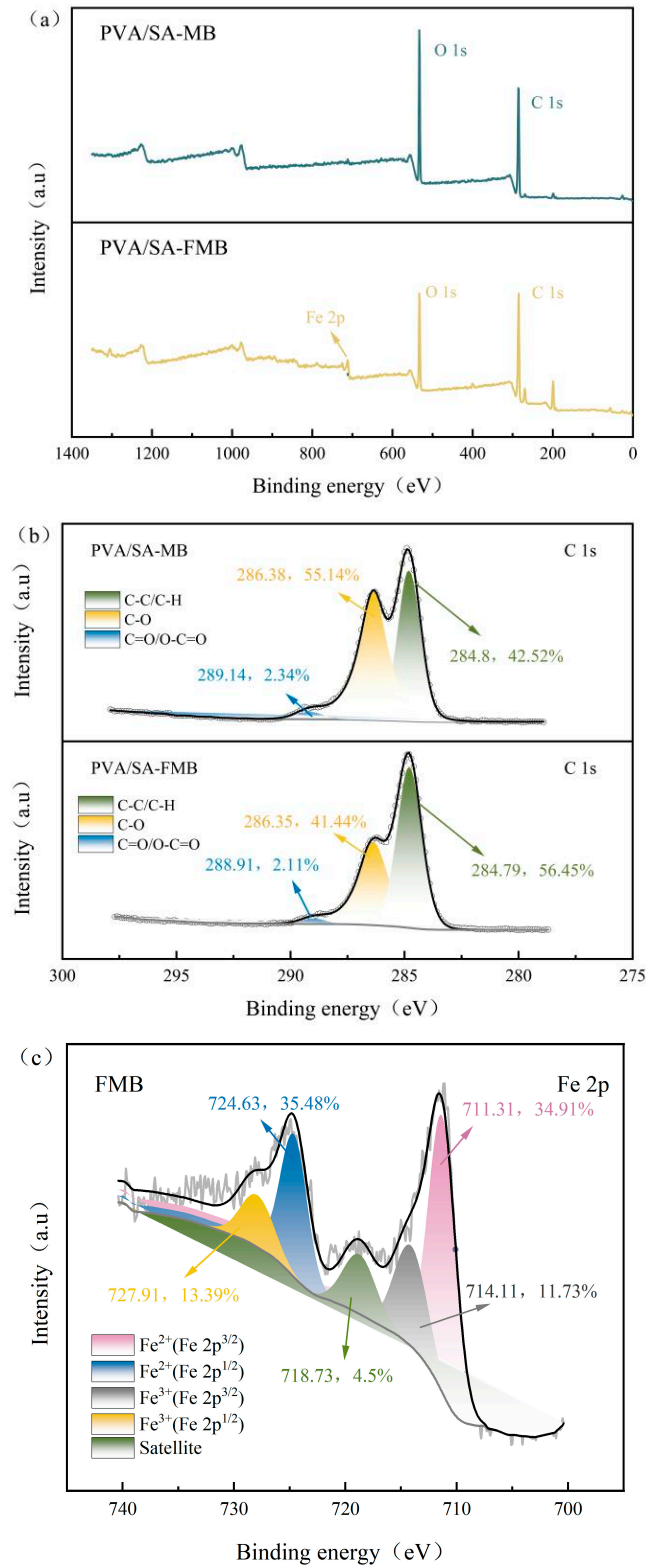

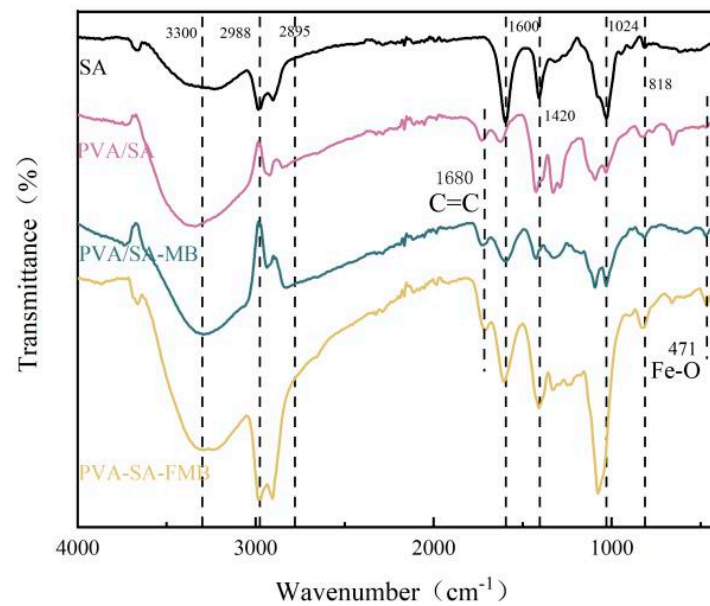**Figure 14.** XPS spectrum of the microsphere. (**a**) Total spectrum; (**b**) C 1s; (**c**) Fe 2p.
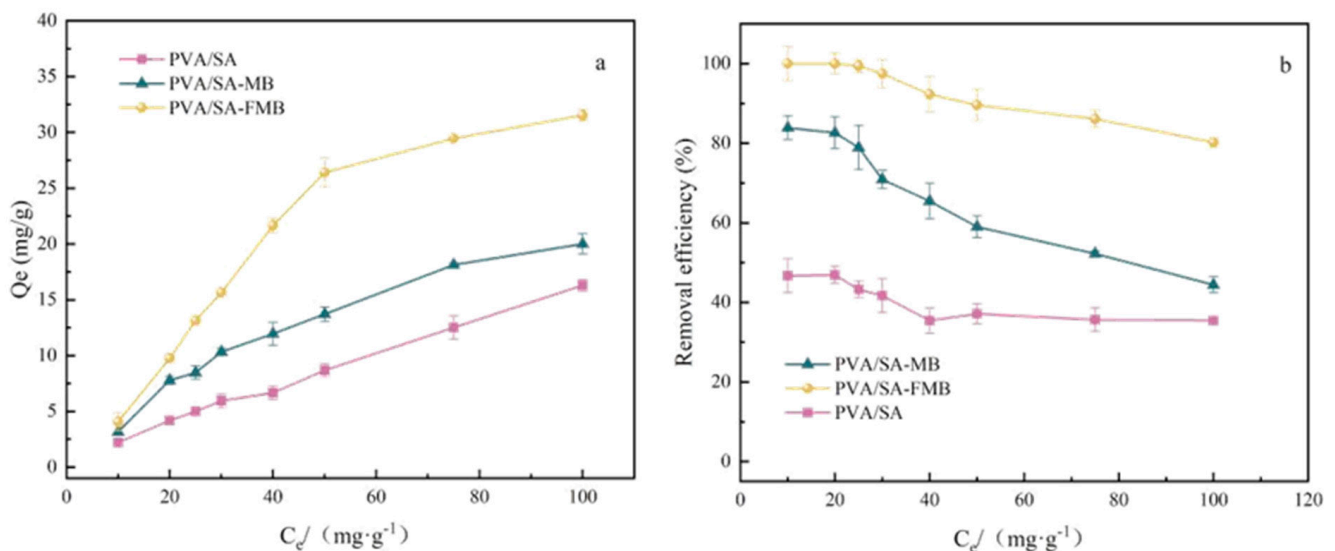
Figure 15. Infrared spectrum of microspheres.

Figure 16. Effect of initial concentration on the adsorption of Cr(VI) by microspheres. (**a**) Qe; (**b**) removal efficiency.

2. Dosage

An experiment was conducted to evaluate the influence of adsorbent dosage on Cr(VI) removal efficiency using 50 mL of simulated wastewater with an initial Cr(VI) concentration of 50 mg/L and a pH of 2. Various dosages of adsorbents (0.05, 0.1, 0.15, 0.2, and 0.25 g) including PVA/SA, PVA/SA-MB, and PVA/SA-FMB, were introduced into conical flasks, which were then agitated in a constant temperature water bath at 25 °C and 140 r/min for 24 h. Following equilibrium, the residual Cr(VI) concentration was determined to assess the adsorbent dosage effect on adsorption capacity, with findings depicted in Figure 17.

The experiment revealed a distinct trend in Cr(VI) removal efficiency relative to adsorbent dosage. With increasing doses of PVA/SA, PVA/SA-MB, and PVA/SA-FMB, a notable decline in adsorption capacity per unit mass was observed, recording reductions of 2.21, 8.3, and 23.36 mg/g, respectively. Despite this, the overall adsorption efficiency for each adsorbent significantly improved by 51.9%, 63.7%, and 44.19%, respectively. This phenomenon is attributed to the presence of unsaturated adsorption sites at lower doses.

As the adsorbent dosage increased, more adsorption sites became available, enhancing the total removal efficiency. A marked increase in Cr(VI) removal efficiency was noted at an adsorbent dose of 3.0 g/L, eventually plateauing at higher doses. This plateau indicates an equilibrium state between Cr(VI) ions and the adsorbent, suggesting that further increases in adsorbent dosage beyond this point do not significantly impact Cr(VI) removal, thereby identifying an optimal adsorption capacity within the tested conditions.
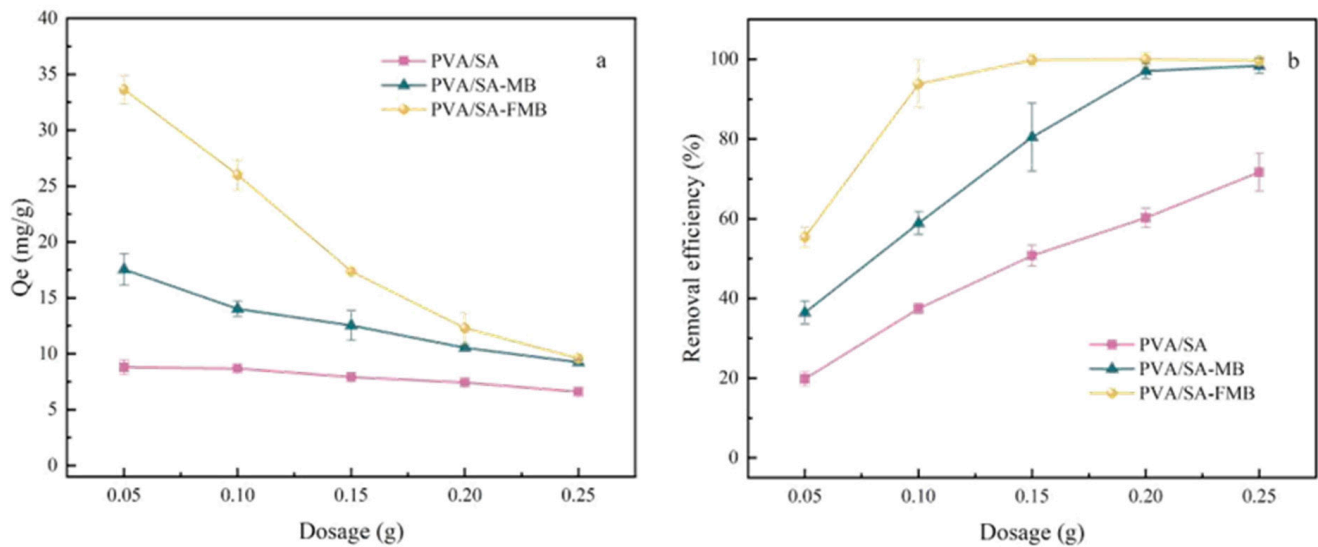
Figure 17. Effect of dosage on adsorption of Cr(VI) by biochar. (**a**) Qe; (**b**) removal efficiency.

3. pH

The response of various adsorbents to the adsorption of Cr(VI) ions is significantly influenced by the pH of the solution. To assess this effect, experiments were conducted across a pH range of 1–10, using an initial Cr(VI) ion concentration of 50.0 mg/L, an adsorbent dosage of 2 g/L, and at a temperature of 25 °C. Figure 18 illustrates the impact of pH on the removal efficiency of Cr(VI) ions by three different adsorbents.
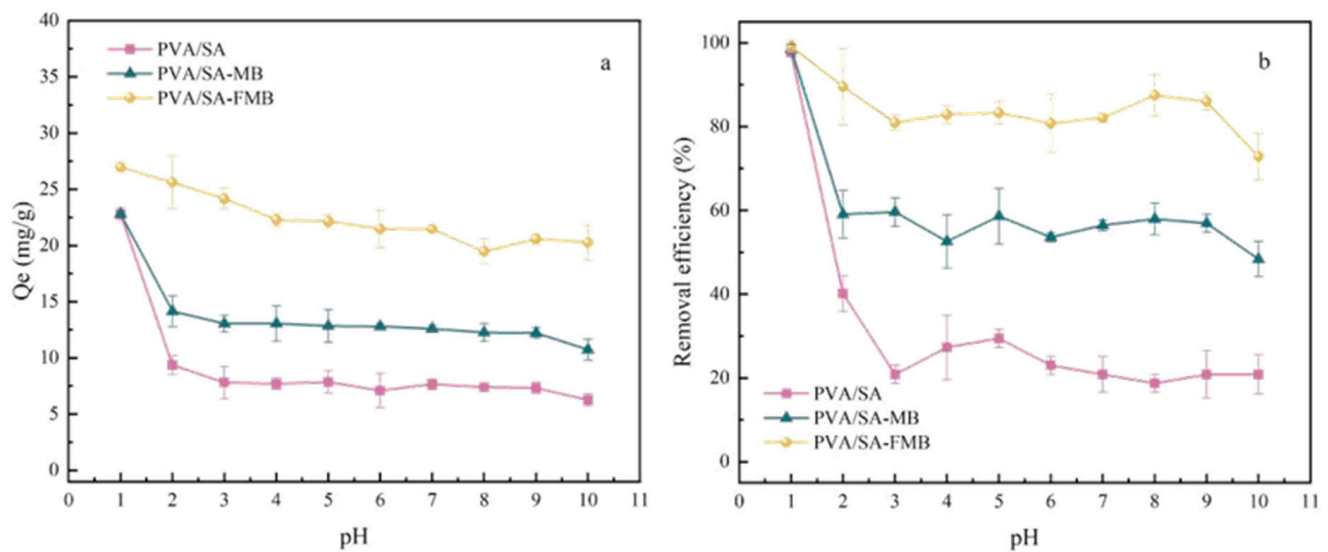

Figure 18. Effect of pH biochar on Cr(VI) adsorption. (**a**) Qe; (**b**) removal efficiency.

The analysis of Cr(VI) adsorption using different adsorbents reveals a consistent trend across the pH spectrum. All adsorbents show enhanced performance under acidic conditions compared to alkaline and neutral environments, with the highest adsorption

capacity occurring at a pH of 1. As the pH increases, the efficiency of Cr(VI) adsorption declines significantly before stabilizing. The reasons for this trend are as follows: (1) At low pH, the adsorbent's positively charged functional groups interact more effectively with the negatively charged dichromate ions, thereby facilitating adsorption. (2) The hydroxyl (-OH) groups on the adsorbent act as electron donors. Under acidic conditions, these groups consume protons (H^+) from the solution, partially reducing Cr(VI) to Cr(III). As the solution becomes less acidic, the availability of H^+ diminishes, adversely affecting the adsorbent's performance [22]. (3) With increasing pH, the concentration of -OH groups increases, leading to competition between the -OH radicals and Cr(VI) ions for adsorption sites on the adsorbent's surface. These observations suggest that electrostatic interactions play a significant role in the adsorption mechanism of Cr(VI) by the microspheres, particularly under acidic conditions.

At a pH of 1, for FMB and PVA/SA-FMB, the capacities are 23.76 mg/g and 26.96 mg/g, respectively. In contrast, for MB and PVA/SA-FMB, the capacities are 22.48 mg/g and 22.81 mg/g, respectively. These values indicate that the addition of PVA/SA positively influences the adsorption capacity, likely due to PVA/SA providing an abundance of H^+ ions in the solution. At the same pH, PVA/SA-FMB always maintains the highest Cr(VI) removal rate and adsorption capacity, and is almost unaffected by the pH value of the solution. This stability is attributed to the presence of a Fe^{3+} and -OH composition buffer pair in PVA/SA-FMB, which effectively counteracts pH fluctuations, ensuring efficient adsorption performance over a wide pH range. Given that the pH of industrial wastewater containing Cr(VI) typically ranges from 2 to 3, the adsorption performance of adsorbents at pH 2 is particularly relevant and noteworthy [23].

3.3.2. Adsorption Kinetics Experiment

To further understand the mechanism of Cr(VI) removal by PVA/SA, PVA/SA-MB, and PVA/SA-FMB, as well as to identify the rate-limiting steps in the adsorption process, this study applied both quasi-first-order and quasi-second-order kinetic models to the kinetic data. Figure 19 displays the time-dependent adsorption curves for Cr(VI) using these adsorbents, with the relevant fitting parameters detailed in Table 6. For PVA/SA, the fit with the quasi-first-order model (correlation coefficient of 0.93918) was more precise than with the quasi-second-order model (0.91584), indicating that the adsorption process of PVA/SA might be primarily influenced by the rate of adsorption and the availability of free sites on the adsorbent surface. In contrast, for PVA/SA-MB and PVA/SA-FMB, the quasi-second-order kinetic model provided a better fit, with model parameters closely matching the observed equilibrium adsorption capacities, suggesting that the adsorption processes for these adsorbents might be related to the number of free sites on the adsorbent surface and the potential forces or chemical bonds formed.

Table 6. The quasi-primary and quasi-secondary kinetic fitting parameters of Cr(VI) adsorption by microspheres.

Microspheres	$Q_e/(mg \cdot g^{-1})$	Quasi-First-Order Kinetics			Quasi-Second-Order Kinetics		
		$Q_t/(mg \cdot g^{-1})$	k_1/min^{-1}	R^2	$Q_t/(mg \cdot g^{-1})$	$k_1/(g \cdot mg^{-1} \cdot min^{-1})$	R^2
PVA/SA	9.34	9.28	0.0053	0.94	11.04	5.29×10^{-4}	0.92
PVA/SA-MB	14.07	13.36	0.0105	0.92	14.52	0.0011	0.95
PVA/SA-FMB	26.03	22.61	0.0277	0.95	24.99	0.0016	0.99

A notable finding is that PVA/SA-FMB exhibited a maximum adsorption capacity of 26.03 mg/g for Cr(VI). Remarkably, within the first 30 min, it achieved an adsorption capacity of 13.7 mg/g, accounting for 52.6% of its total capacity. This capacity increased to 76.2% (20.5 mg/g) in the following two hours. These results demonstrate the high number

of active sites on PVA/SA-FMB, enabling rapid interaction with Cr(VI) and showcasing its exceptional efficiency in swiftly removing Cr(VI).
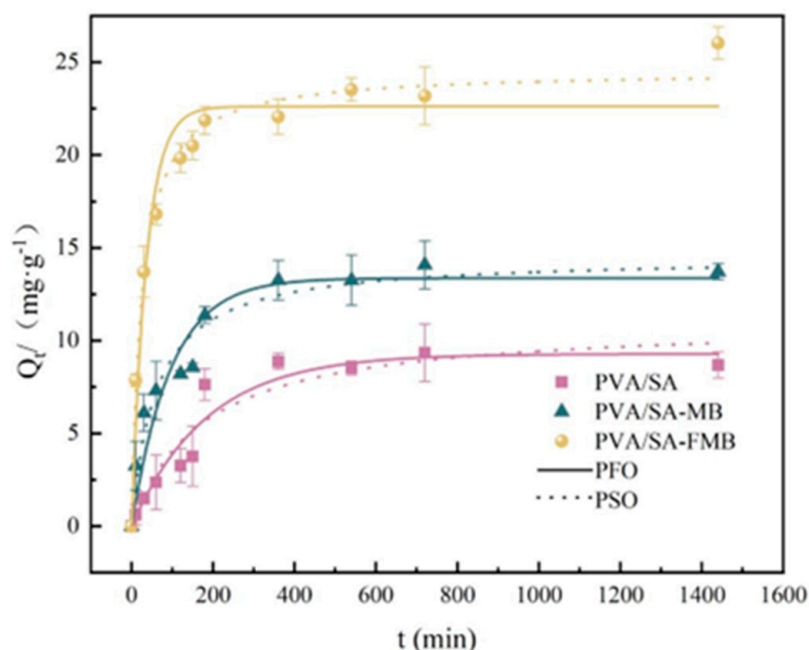

Figure 19. Fitting curve of adsorption kinetics of Cr(VI) by microspheres.

Applying the Weber–Morris intraparticle diffusion model to evaluate Cr(VI) adsorption by PVA/SA, PVA/SA-MB, and PVA/SA-FMB, the relevant fitting parameters detailed in Table 7. Figure 20 illustrates that the model's fitted lines do not intersect the origin. This observation signifies that intraparticle diffusion alone does not constitute the sole rate-limiting step [24]. The adsorption mechanism encompasses two distinct phases: boundary diffusion and intraparticle diffusion, with the initial boundary diffusion phase exhibiting more pronounced slopes and correlation coefficients. This indicates that boundary diffusion acts as the primary rate-limiting step in Cr(VI) removal by these adsorbents.

Table 7. Fitting parameters of adsorption particle diffusion for Cr(VI) by microspheres.

Microspheres	R_{d1}^2	$k_{id1}/$ $(mg \cdot g^{-1} \cdot h^{-0.5})$	C'_1 $(mg \cdot g^{-1})$	R_{d2}^2	$k_{id2}/$ $(mg \cdot g^{-1} \cdot h^{-0.5})$	C'_2 $(mg \cdot g^{-1})$
PVA/SA	0.76865	0.53247	1.51448	0.0366	0.01627	8.83264
PVA/SA-MB	0.89788	0.63434	1.86151	0.38649	0.01919	12.99951
PVA/SA-FMB	0.94667	1.26448	5.58574	0.94309	0.19211	18.76642

3.3.3. Isothermal Adsorption Experiment

Analyzing the adsorption capacity of PVA/SA, PVA/SA-MB, and PVA/SA-FMB for Cr(VI) using Langmuir and Freundlich models (Figure 21) reveals nuanced insights into their adsorption mechanisms. The model parameters are listed in Table 8. The Langmuir model slightly favored PVA/SA, indicating adsorption involves both monolayer and multilayer processes. In contrast, the Freundlich model better suited PVA/SA-MB and PVA/SA-FMB, suggesting a preference for multilayer adsorption. Freundlich isotherm calculations positioned PVA/SA-FMB with the highest adsorption capacity at around 60 mg/g, outperforming PVA/SA-MB. The Freundlich constant $1/n$ values for all adsorbents were below 1, denoting favorable Cr(VI) adsorption, with PVA/SA-FMB showing the lowest $1/n$ value, indicating a more homogeneous adsorption site distribution [25]. This underscores PVA/SA-FMB microbeads' enhanced efficacy for Cr(VI) removal.
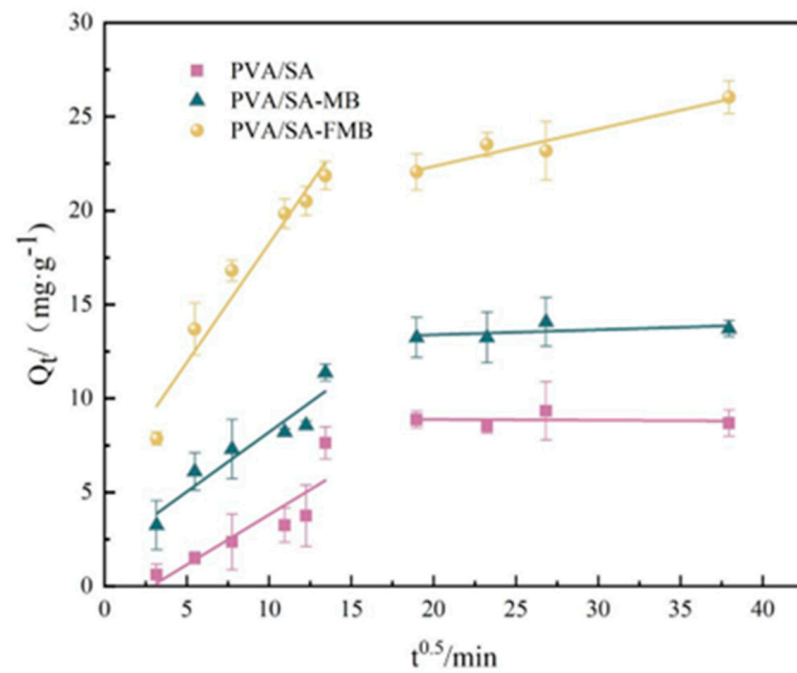
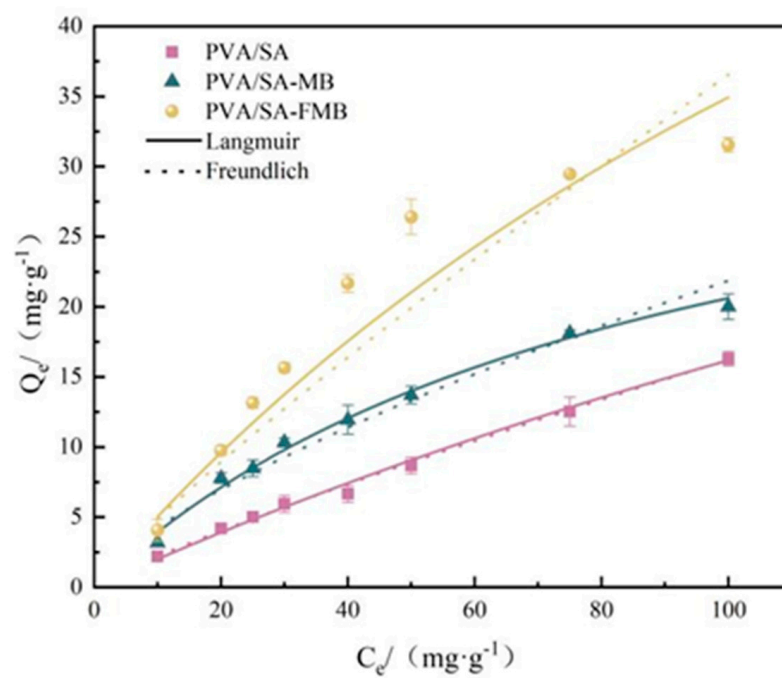**Figure 20.** Particle diffusion fitting curve of microspheres for Cr(VI).

Figure 21. Isothermal adsorption fitting curve of Cr(VI) by microspheres.

Table 8. Isotherm model parameters of Cr(VI) adsorption by microspheres.

Microspheres	Langmuir				Freundlich		
	$Q_m/(mg \cdot g^{-1})$	$K_L/(L \cdot mg^{-1})$	n	R^2	$K_F/(L \cdot mg^{-1})$	n	R^2
PVA/SA	46.81	0.0052	1.51–1.05	0.97	0.38	1.23	0.96
PVA/SA-MB	48.86	0.0079	1.79–1.08	0.99	0.57	1.25	0.98
PVA/SA-FMB	59.93	0.0107	2.08–1.11	0.99	1.44	1.47	0.98

3.3.4. Adsorption Cycle Regeneration Experiment

Figure 22 depicts the adsorption efficiency of PVA/SA, PVA/SA-MB, and PVA/SA-FMB microbeads across five adsorption–desorption cycles, revealing a 5% decrease in removal rates after the initial cycle for each microsphere type. This decline is linked to the release of non-crosslinked Fe^{3+} ions into the desorption solution, reducing the adsorption site density on the microspheres. Subsequent cycles showed stabilization in adsorption capacity, with a slight efficiency decrease attributed to diminished availability of hydroxyl groups crucial for Cr(VI) reduction [26]. Remarkably, PVA/SA-FMB maintained a Cr(VI) removal rate above 90%, outperforming conventional biological carbon. This performance highlights PVA/SA-FMB's efficacy and potential as a superior adsorbent for Cr(VI) remediation in water.
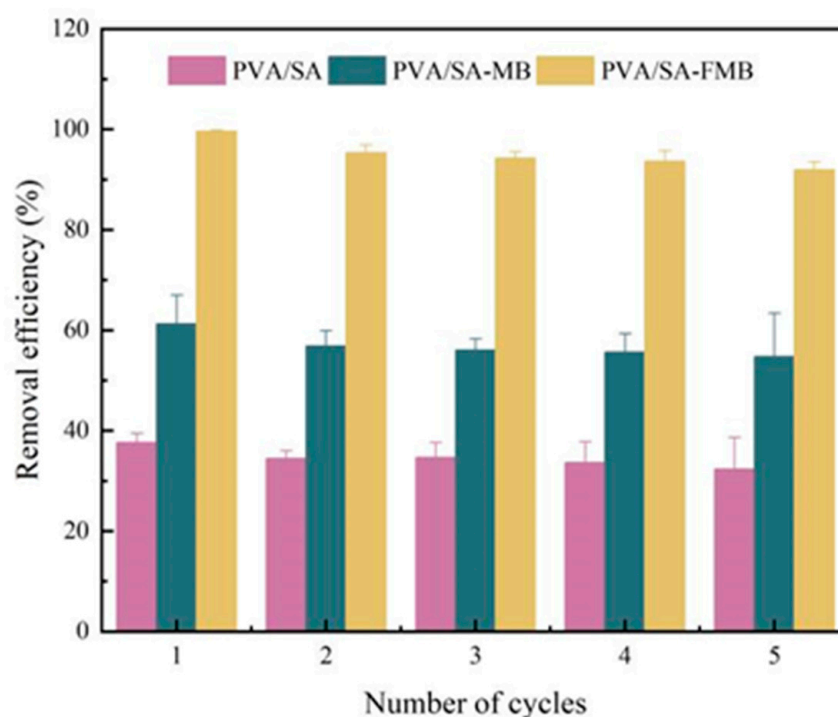

Figure 22. Performance of Cr(VI) adsorption by recycling microspheres.

3.4. Exploration of Adsorption Mechanism

3.4.1. Electrostatic Adsorption

Under acidic conditions, the surface functional groups of the microspheres, primarily hydroxyl (-OH) and carboxyl (-COOH), interact with hydrogen ions (H^+), leading to an increased polarization of these groups. The -OH groups can attract H^+ to form more polarized hydroxyl groups, enhancing their positive character, and -COOH groups can release H^+ to the solution, slightly increasing the surface positive charge by exposing the positively charged hydrogen of the carboxyl group. These modifications enhance the electrostatic attraction between the microsphere and negatively charged Cr(VI) species. This electrostatic interaction facilitates the adsorption of Cr(VI) onto the microsphere surface and may contribute to its reduction to the less toxic Cr(III) species [27].

$$4CrO_4^{2-} + 20H^+ + 3C^+ \rightarrow 3CO_2 + 4Cr^{3+} + 10H_2O \tag{2}$$
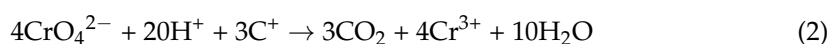
3.4.2. FTIR Analysis after Cr(VI) Adsorption

Fourier transform infrared spectroscopy analysis of PVA/SA-FMB microspheres, as illustrated in Figure 23, demonstrates consistent absorption peaks within the 400–4000 cm^{-1} range before and after adsorption, indicating the enhanced stability of SA-embedded adsorbents over traditional biochar. Crucial functional groups, including -OH, C=O, -COOH,

C=C, and C-H, are pivotal in Cr(VI) adsorption and reduction. The -OH group's stretching vibration peak at 3300 cm^{-1} diminishes post-adsorption, suggesting complexation or ion exchange with Cr(VI). Changes at the 1600 cm^{-1} peak reflect the C=O interactions with Cr(VI), indicative of redox activities [28,29]. Additionally, shifts at 1680 and 1420 cm^{-1} point to redox reactions involving C=C or carboxyl groups, while a weakened C-H peak implies the role of polycyclic aromatic hydrocarbons (PAHs) as proton donors in Cr(VI) reduction [30,31].
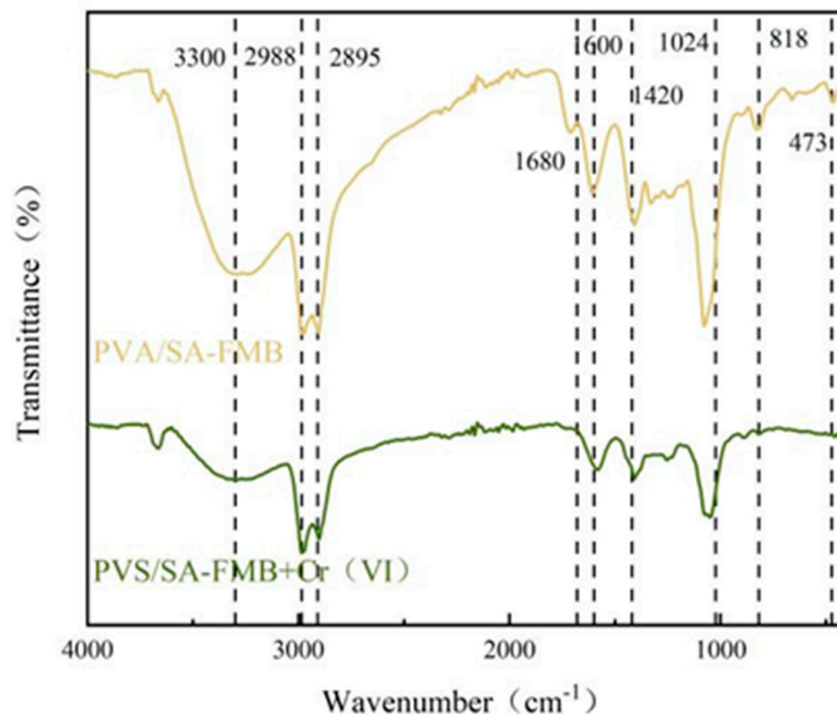
Figure 23. Infrared spectra of Cr(VI) adsorbed by PCA/SA-FMB.

3.4.3. XPS Analysis after Cr(VI) Adsorption

Figure 24a presents the XPS spectrum of Cr(VI) adsorbed by microspheres, illustrating a distinct Cr absorption peak and confirming successful Cr adsorption. In Figure 24b, the Cr 2p spectrum post-adsorption reveals four peaks at binding energies of 577.31 eV, 584.47 eV, 580.15 eV, and 589.31 eV for Cr(III) and Cr(VI) states, with a Cr(III) to Cr(VI) ratio of 79.19% to 20.81%, signifying a partial reduction of Cr(VI) to Cr(III). Conversely, PVA/SA-FMB's Cr 2p XPS spectrum is dominated by Cr(III) peaks, highlighting the composite's superior reduction capability, attributed to surface Fe(III) enhancing Cr(VI) reduction and facilitating electron transfer with modified biochar.

Figure 24c examines C 1s post-adsorption, showing shifts in C-O and C=O/O-C=O functional groups, indicating their role in Cr(VI) adsorption through hydrogen bonding and complexation. These observations underscore the significance of these functional groups in heavy metal complexation on the surfaces of PVA/SA-MB and PVA/SA-FMB microspheres, aligning with infrared analysis findings. The specific reaction process is as follows:

$$\text{C-OFe}^{2+} \text{ HCrO}_4^- \rightarrow \text{C-OFeHCrO}_4^+ \tag{3}$$

$$\text{C-COOH} + \text{HCrO}_4^- + \text{H}^+ \rightarrow \text{C-COOH}_2\text{HCrO}_4 \tag{4}$$

$$\text{C-OH} + \text{HCrO}_4 + \text{H}^+ \rightarrow \text{C-OH}_2\text{HCrO}_4 \tag{5}$$

$$\text{C-COOH} + \text{Cr(OH)}^{2+} \rightarrow \text{C-COOr(OH)}^{2+} + \text{H}^+ \tag{6}$$

$$\text{C-OH} + \text{Cr(OH)}^{2+} \rightarrow \text{C-OCr(OH)}^{2+} + \text{H}^+ \tag{7}$$
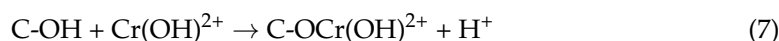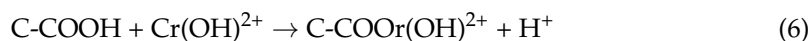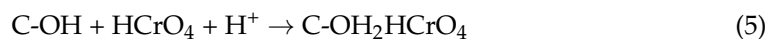
Figure 24d illustrates a shift in the Fe(II) and Fe(III) content following Cr(VI) adsorption by PVA/SA-FMB, with Fe(II) absorption peaks decreasing from 80.62% to 68.78% and Fe(III) peaks increasing from 19.64% to 31.22%. This variation is due to Fe(II) donating electrons to reduce Cr(VI) to Cr(III), while some Fe(II) is oxidized to Fe(III), which is then adsorbed onto the PVA/SA-FMB surface. The increase in the Fe(III) content highlights its role as an electron shuttle, facilitating further Cr(VI) removal. This change emphasizes the crucial involvement of redox reactions in the adsorption mechanism of Cr(VI) onto PVA/SA-FMB.
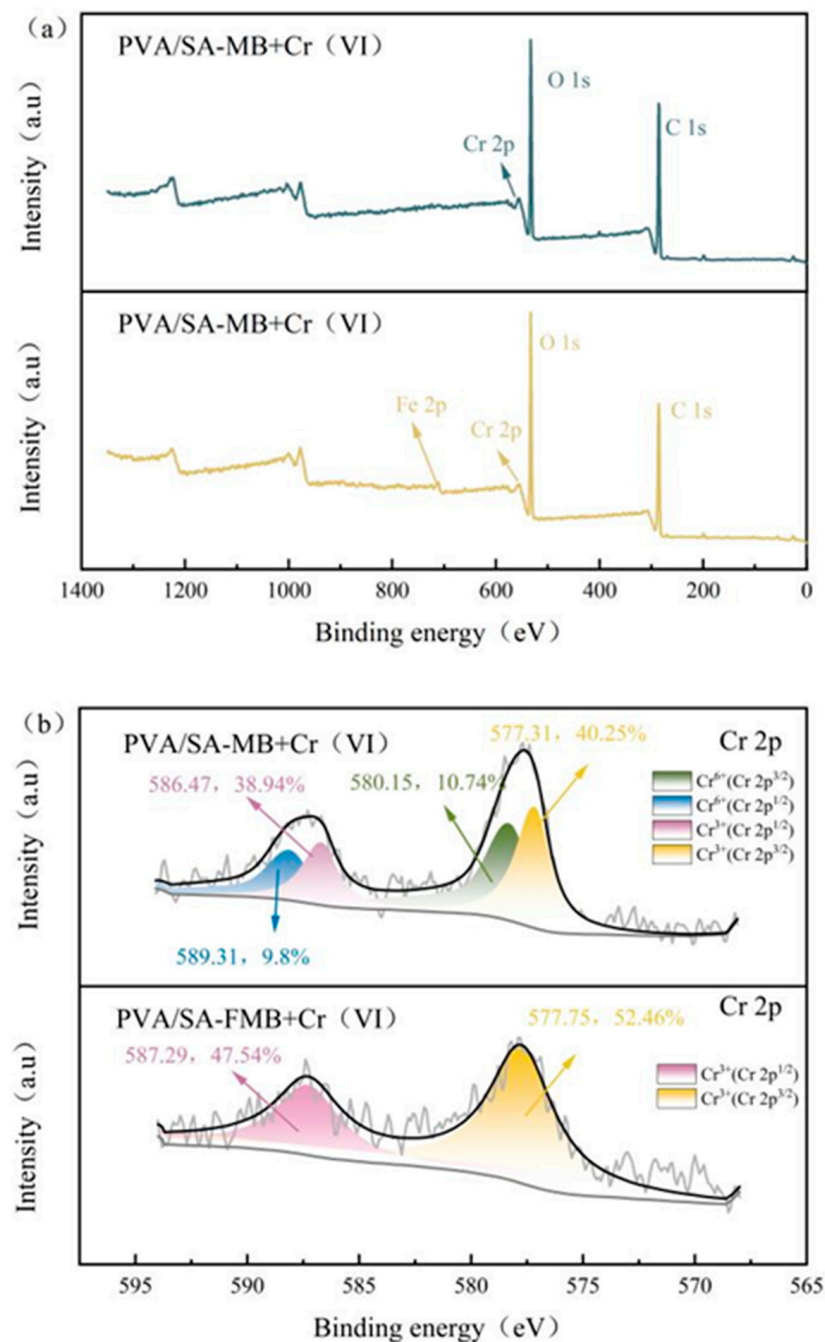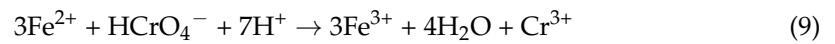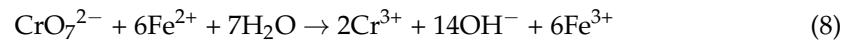
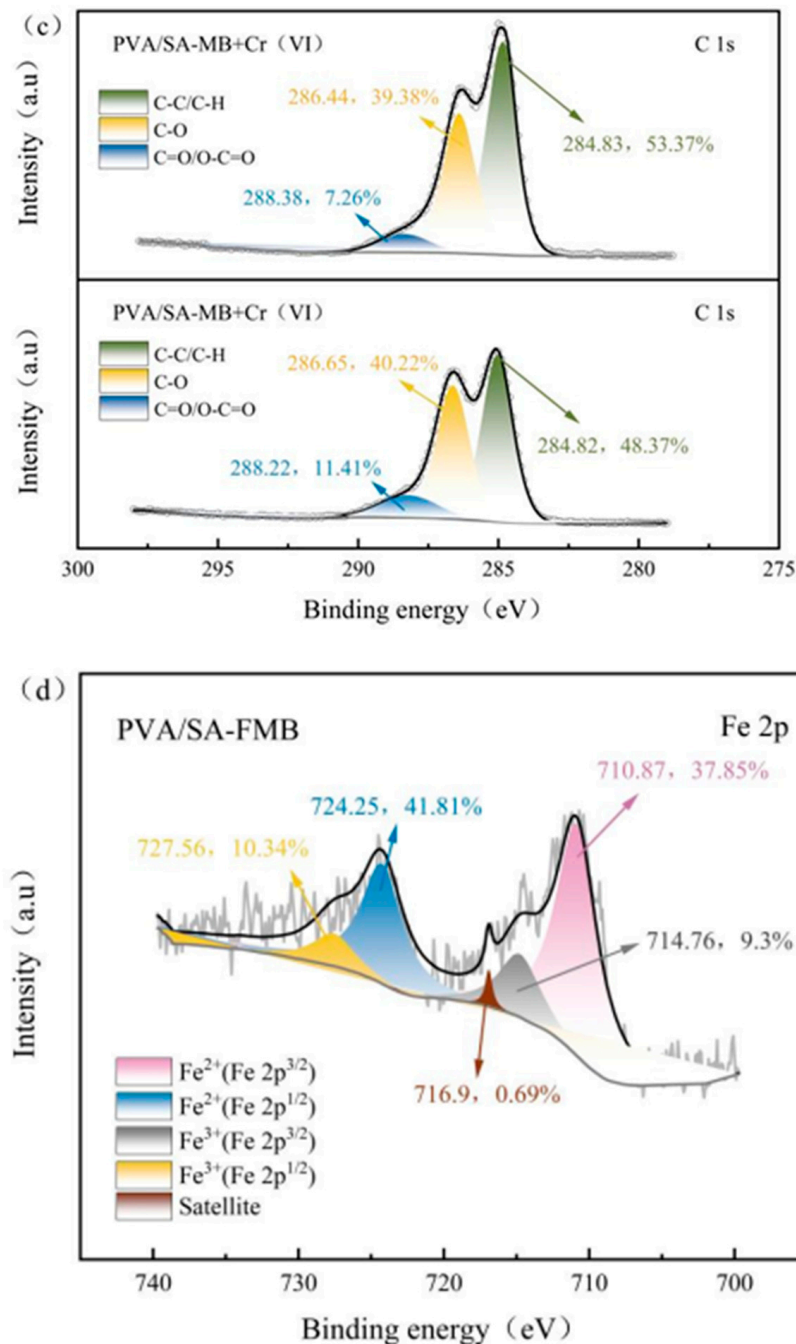$$CrO_7^{2-} + 6Fe^{2+} + 7H_2O \rightarrow 2Cr^{3+} + 14OH^- + 6Fe^{3+} \tag{8}$$

$$3Fe^{2+} + HCrO_4^- + 7H^+ \rightarrow 3Fe^{3+} + 4H_2O + Cr^{3+} \tag{9}$$

Figure 24. *Cont.*

Figure 24. XPS spectrum after Cr(VI) adsorption using microspheres. (**a**) Total spectrum; (**b**) Cr 2p; (**c**) C 1s; (**d**) Fe 2p.

4. Conclusions

The optimal preparation conditions for the PVA/SA-FMB composite were established with a SA concentration of 0.73 wt%, PVA concentration of 3 wt%, FMB mass of 0.31 g, and a CaCO$_3$ mass of 1 g, ensuring the effective incorporation of FMB into the polymeric matrix. Adsorption experiments conducted at 25 °C and a pH of 2 revealed that while Cr(VI) adsorption onto PVA/SA adhered to the quasi-first-order kinetic and Langmuir isothermal model, indicative of physical multilayer adsorption, the adsorption onto PVA/SA-MB and PVA/SA-FMB followed the quasi-second-order kinetic model and Freundlich isotherm model, suggesting a more complex, multilayer chemisorption process. SEM analysis showed that PVA/SA microspheres presented a smooth surface, in contrast to PVA/SA-MB and PVA/SA-FMB, which exhibited numerous bundle struc-

tures typical of biochar, with PVA/SA-FMB displaying a notably rougher and more porous surface than its PVA/SA-MB counterpart. Further analyses, including FTIR, XPS, and XRD, identified various functional groups on the microsphere surfaces and highlighted the inclusion of Fe_2O_3 and FeO in different valence states within the FMB. BET analysis confirmed the presence of micropores and mesopores across all microsphere types, supporting their potential for enhanced adsorption capacities. Collectively, these findings underscore the multilayer adsorption character of Cr(VI) by PVA/SA-MB and PVA/SA-FMB, driven by a synergy of electrostatic interactions, redox reactions, and complexation, marking a significant advancement in the development of efficient adsorption materials for heavy metal removal from aqueous solutions.

Author Contributions: Conceptualization, J.Z.; software, Z.X.; formal analysis, L.J.; investigation, Z.X.; data curation, L.J.; methodology and writing—original draft preparation, J.R.; writing—review and editing, C.T.; supervision, J.L.; resources, validation, W.W.; project administration, and funding acquisition, J.Z. All authors have read and agreed to the published version of the manuscript.

Data Availability Statement: Data are contained within the article.

References

1. Rashid, R.; Shafiq, I.; Akhter, P.; Iqbal, M.J.; Hussain, M. A state-of-the-art review on wastewater treatment techniques: The effectiveness of adsorption method. *Environ. Sci. Pollut. Res.* **2021**, *28*, 9050–9066. [CrossRef]
2. Pakade, V.E.; Tavengwa, N.T.; Madikizela, L.M. Recent advances in hexavalent chromium removal from aqueous solutions by adsorptive methods. *RSC Adv.* **2019**, *9*, 26142–26164. [CrossRef] [PubMed]
3. King, A.H. Brown Seaweed Extracts (Alginates). In *Food Hydrocolloids*; CRC Press: Boca Raton, FL, USA, 2019; pp. 115–188.
4. Rhim, J.W. Physical and mechanical properties of water resistant sodium alginate films. *LWT-Food Sci. Technol.* **2004**, *37*, 323–330. [CrossRef]
5. Gao, X.; Guo, C.; Hao, J.; Zhao, Z.; Long, H.; Li, M. Adsorption of heavy metal ions by sodium alginate based adsorbent-a review and new perspectives. *Int. J. Biol. Macromol.* **2020**, *164*, 4423–4434. [CrossRef] [PubMed]
6. Wróblewska-Krepsztul, J.; Rydzkowski, T.; Michalska-Pożoga, I.; Thakur, V.K. Biopolymers for Biomedical and Pharmaceutical Applications: Recent Advances and Overview of Alginate Electrospinning. *Nanomaterials* **2019**, *9*, 404. [CrossRef] [PubMed]
7. Thakur, S.; Sharma, B.; Verma, A.; Chaudhary, J.; Tamulevicius, S.; Thakur, V.K. Recent progress in sodium alginate based sustainable hydrogels for environmental applications. *J. Clean. Prod.* **2018**, *198*, 143–159. [CrossRef]
8. Zhang, H.; Han, X.; Liu, J.; Wang, M.; Zhao, T.; Kang, L.; Zhong, S.; Cui, X. Fabrication of modified alginate-based biocomposite hydrogel microspheres for efficient removal of heavy metal ions from water. *Colloids Surf. A Physicochem. Eng. Asp.* **2022**, *651*, 129736. [CrossRef]
9. Kaklamani, G.; Cheneler, D.; Grover, L.M.; Adams, M.J.; Bowen, J. Mechanical properties of alginate hydrogels manufactured using external gelation. *J. Mech. Behav. Biomed. Mater.* **2014**, *36*, 135–142. [CrossRef] [PubMed]
10. Mahou, R.; Borcard, F.; Crivelli, V.; Montanari, E.; Passemard, S.; Noverraz, F.; Gerber-Lemaire, S.; Bühler, L.; Wandrey, C. Tuning the properties of hydrogel microspheres by adding chemical cross-linking functionality to sodium alginate. *Chem. Mater.* **2015**, *27*, 4380–4389. [CrossRef]
11. Alshehari, A.M.; Salim, E.; Oraby, A.H. Structural, optical, morphological and mechanical studies of polyethylene oxide/sodium alginate blend containing multi-walled carbon nanotubes. *J. Mater. Res. Technol.* **2021**, *15*, 5615–5622. [CrossRef]
12. Xiang, X.; Yi, X.; Zheng, W.; Li, Y.; Zhang, C.; Wang, X.; Chen, Z.; Huang, M.; Ying, G.G. Enhanced biodegradation of thiamethoxam with a novel polyvinyl alcohol (PVA)/sodium alginate (SA)/biochar immobilized Chryseobacterium sp H5. *J. Hazard. Mater.* **2023**, *443*, 130247. [CrossRef]
13. Zain, N.; Suhaimi, M.S.; Idris, A. Development and modification of PVA–alginate as a suitable immobilization matrix. *Process Biochem.* **2011**, *46*, 2122–2129. [CrossRef]
14. Idris, A.; Zain NA, M.; Suhaimi, M.S. Immobilization of Baker's yeast invertase in PVA–alginate matrix using innovative immobilization technique. *Process Biochem.* **2008**, *43*, 331–338. [CrossRef]
15. Lv, X.; Jiang, G.; Xue, X.; Wu, D.; Sheng, T.; Sun, C.; Xu, X. Fe_0-Fe_3O_4 nanocomposites embedded polyvinyl alcohol/sodium alginate beads for chromium (VI) removal. *J. Hazard. Mater.* **2013**, *262*, 748–758. [CrossRef]
16. Ramdhan, T.; Ching, S.H.; Prakash, S.; Bhandari, B. Time dependent gelling properties of cuboid alginate gels made by external gelation method: Effects of alginate-$CaCl_2$ solution ratios and pH. *Food Hydrocoll.* **2019**, *90*, 232–240. [CrossRef]

17. Hameed, B.H.; Din, A.M.; Ahmad, A.L. Adsorption of methylene blue onto bamboo-based activated carbon: Kinetics and equilibrium studies. *J. Hazard. Mater.* **2007**, *141*, 819–825. [CrossRef] [PubMed]

18. Crini, G.; Badot, P.M. Application of chitosan, a natural aminopolysaccharide, for dye removal from aqueous solutions by adsorption processes using batch studies: A review of recent literature. *Prog. Polym. Sci.* **2008**, *33*, 399–447. [CrossRef]

19. Kumar, L.; Kumar, P.; Narayan, A.; Kar, M. Rietveld analysis of XRD patterns of different sizes of nanocrystalline cobalt ferrite. *Int. NanoLett.* **2013**, *3*, 8. [CrossRef]

20. Fei, Y.; Yong, L.; Sheng, H.; Ma, J. Adsorptive removal of ciprofloxacin by sodium alginate/graphene oxide composite beads from aqueous solution. *J. Colloid Interface Sci.* **2016**, *484*, 196–204. [CrossRef] [PubMed]

21. Fan, H.; Ma, X.; Zhou, S.; Huang, J.; Liu, Y.; Liu, Y. Highly efficient removal of heavy metal ions by carboxymethyl cellulose-immobilized Fe3O4 nanoparticles prepared via high-gravity technology. *Carbohydr. Polym.* **2019**, *213*, 39–49. [CrossRef] [PubMed]

22. Yan, L.; Dong, F.-X.; Li, Y.; Guo, P.-R.; Kong, L.-J.; Chu, W.; Diao, Z.-H. Synchronous removal of Cr(VI) and phosphates by a novel crayfish shell biochar-Fe composite from aqueous solution: Reactivity and mechanism. *J. Environ. Chem. Eng.* **2022**, *10*, 107396. [CrossRef]

23. Chen, J.H.; Xing, H.T.; Guo, H.X.; Weng, W.; Hu, S.R.; Li, S.X.; Huang, Y.H.; Sun, X.; Su, Z.B. Investigation on the adsorption properties of Cr (VI) ions on a novel graphene oxide (GO) based composite adsorbent. *J. Mater. Chem. A* **2014**, *2*, 12561–12570. [CrossRef]

24. Srivastava, S.; Tyagi, R.; Pant, N. Pant, Adsorption of heavy metal ions on carbonaceous material developed from the waste slurry generated in local fertilizer plants. *Water Res.* **1989**, *23*, 1161–1165. [CrossRef]

25. Zhang, W.; Zhang, S.; Wang, J.; Wang, M.; He, Q.; Song, J.; Wang, H.; Zhou, J. Hybrid functionalized chitosan-Al_2O_3@SiO_2 composite for enhanced Cr(VI) adsorption. *Chemosphere* **2018**, *203*, 188. [CrossRef] [PubMed]

26. Song, L.; Liu, F.; Zhu, C.; Li, A. Facile one-step fabrication of carboxymethyl cellulose based hydrogel for highly efficient removal of Cr(VI) under mild acidic condition. *Chem. Eng. J.* **2019**, *369*, 641–651. [CrossRef]

27. Park, D.; Yun, Y.-S.; Park, J.M. The past, present, and future trends of biosorption. *Biotechnol. Bioprocess Eng.* **2005**, *10*, 86–102. [CrossRef]

28. Zhang, S.; Lyu, H.; Tang, J.; Song, B.; Zhen, M.; Liu, X. A novel biochar supported CMC stabilized nano zero-valent iron composite for hexavalent chromium removal from water. *Chemosphere* **2019**, *217*, 686–694. [CrossRef]

29. Wan, Z.; Cho, D.-W.; Tsang, D.C.; Li, M.; Sun, T.; Verpoort, F. Concurrent adsorption and micro-electrolysis of Cr(VI) by nanoscale zerovalent iron/biochar/Ca-alginate composite. *Environ. Pollut.* **2019**, *247*, 410–420. [CrossRef]

30. Yu, Y.; An, Q.; Jin, L.; Luo, N.; Li, Z.; Jiang, J. Unraveling sorption of Cr (VI) from aqueous solution by $FeCl_3$ and $ZnCl_2$-modified corn stalks biochar: Implicit mechanism and application. *Bioresour. Technol.* **2020**, *297*, 122466. [CrossRef]

31. Yusuff, A.S.; Lala, M.A.; Thompson-Yusuff, K.A.; Babatunde, E.O. $ZnCl_2$-modified eucalyptus bark biochar as adsorbent: Preparation, characterization and its application in adsorption of Cr (VI) from aqueous solutions. *S. Afr. J. Chem. Eng.* **2022**, *42*, 138–145. [CrossRef]